

Searching for binary black hole mergers with deep learning in Advanced LIGO's third observing run

Damon Beveridge,^{1,*} Alistair McLeod,^{1,†} Linqing Wen,^{1,‡} Weichangfeng Guo,¹ and Andreas Wicenc²

¹*Department of Physics, The University of Western Australia,
35 Stirling Highway, Crawley, WA 6009, Australia*

²*International Centre for Radio Astronomy Research,
The University of Western Australia M468, 35 Stirling Hwy, Crawley, WA 6009, Australia*
(Dated: December 5, 2025)

The detection of gravitational waves from compact binary coalescences has provided significant insights into our Universe, and the discovery of new and unique gravitational wave candidates from independent searches remains an ongoing field of research. In this work, we built a hybrid search pipeline that combines matched filtering and deep learning to identify stellar-mass binary black hole candidates from detector strain data. We first present results from a targeted injection study to benchmark the sensitivity of our method and compare it with existing search pipelines. We demonstrate that our hybrid approach has comparable sensitivity for injections with a source-frame chirp mass greater than $25 M_{\odot}$, and below this threshold our sensitivity drops off for signals with a network SNR less than 15. We also observe that our search method can identify a significant population of unique candidates. Furthermore, we conduct an offline search for gravitational wave candidates in the third observing run of the LIGO-Virgo-KAGRA Collaboration (LVK), yielding 31 candidates previously reported by the LVK with a probability of astrophysical origin $p_{\text{astro}} \geq 0.5$. We identify two other candidates: one previously reported only in a search conducted by the Institute for Advanced Study, and one previously unreported promising new candidate with a p_{astro} of 0.63. This unique candidate has a high chirp mass and a high probability that the primary black hole is an intermediate-mass black hole.

I. INTRODUCTION

The LIGO-Virgo-KAGRA collaboration (LVK) [1] has ushered in an era of routine observations of gravitational waves (GWs) produced through compact binary mergers. Since the first detection in 2015, there have been published results from three completed observing runs (O1-O3) and one partial observing run (O4a) using the second-generation of gravitational-wave observatories, including the Hanford and Livingston LIGO observatories [2], Advanced Virgo [3] and KAGRA [4]. Between observing runs, upgrades to the detectors have increased the rate of compact binary merger observations, resulting in over 218 observations at the end of O4a [5–9]. The majority of these candidates are the result of binary black hole (BBH) mergers, with two binary neutron star (BNS) mergers [10, 11] and eight neutron star-black hole (NSBH) mergers [7–9, 12–14]. Since O4a, the fourth observing run (O4) has continued and has reported over 150 significant candidate events, as of the time of writing, in low-latency through the Gravitational-Wave Candidate Event Database (GraceDB)¹, NASA's General Coordinates Network², and the Scalable Cyberinfrastructure to support Multi-Messenger Astrophysics (SCiMMA) project³ [15]. These alerts encourage follow-

up efforts for electromagnetic observation similar to how the first BNS event, GW170817, was observed by electromagnetic observatories [16]. Increases in the observed populations of each compact binary source type and the observation of exceptional events, such as the massive GW190521 merger [17] and the loud GW250114 merger [18], are starting to inform source type populations, merger rates and formation scenarios [19–22], and verify tests of general relativity [23].

With the public release of LIGO and Virgo data, other groups have conducted offline analyses searching for GW signals [24–56]. These searches have reinforced the LVK's results and reported additional candidate events. The most notable of these catalogs of events are the Open Gravitational-Wave Catalog (OGC) series [24–27] and the Institute for Advanced Study (IAS) series [39–43], which search over the first three observing runs for which public data is available. The additional searches generally introduce new ranking statistics for a given search pipeline that improve the search sensitivity, such as for the PyCBC-KDE [38] and cWB [47] searches, or they introduce novel techniques for the method of detecting a merger; for example, the AresGW [53] and Aframe [55] searches use deep-learning models to identify BBH events. The AresGW (Aframe) search identified 52 (41) events in O3, including 39 (38) GWTC-3 candidates, 5 (3) candidates from other catalogs, and 8 (0) unique detections. These catalogs overlap significantly in the candidate events they identify, which are generally events in the LVK's Gravitational Wave Transient Catalogs (GWTC) [5–8], and only 10 candidates have been identified by multiple independent searches outside of the

* damon.beveridge@uwa.edu.au

† alistair.mcleod@research.uwa.edu.au

‡ linqing.wen@uwa.edu.au

¹ <https://gracedb.ligo.org/>

² <https://gcn.nasa.gov/>

³ <https://scimma.org/>

GWTC candidate events in O3.

In this work, we build upon a prior feasibility study that combined matched filtering with a deep-learning model to identify BBH mergers from the signal-to-noise ratio (SNR) time series, using simulated Gaussian strain with injected glitches [57]. We previously demonstrated this method to be feasible for identifying BNS signals injected in O3 public data and the LVK candidate events GW170817 and GW190425 [58]. Here, we apply the method proposed in Ref. [57] for the first time to detect BBH signals in O3 data from the LIGO Hanford and Livingston detectors, and evaluate the detection sensitivity of our search pipeline relative to existing LVK search pipelines. We present results from an offline search for candidate events in the publicly available O3 data, identifying 33 candidate events that exceed our detection threshold—defined as a probability of astrophysical origin, p_{astro} , greater than or equal to 0.5 and a false alarm rate (FAR) below 2 per day, which is consistent with the LVK collaboration criteria [8]. There are 90 candidates in the GWTC-3 catalog; however, only 63 are considered detectable by the O3 offline search in this paper. Of the 33 detected candidates, 31 match those in the LVK’s GWTC-3 catalog [8], including the NSBH candidate GW190814. The remaining two candidates detected by our search include one that coincides with the IAS search that incorporates higher-order harmonics [43], and one that represents a new candidate event not previously reported. We also demonstrate that our detected and missed candidates coincide with the populations of detected and missed injections from our sensitivity analyses, and we have no missed candidates that we expect to identify based on high SNRs and being within our most sensitive mass regions.

In Sec. II, we discuss our search method and deep learning model in detail, including how it differs from Ref. [57], and how we construct our FAR and p_{astro} search statistics. In Sec. III, we apply our search pipeline to a set of signal injections placed into the O3 data and compare our sensitivity and recovered populations to the existing LVK search pipelines. Lastly, Sec. IV discusses the results of our offline search of O3 data, including the detected and missed populations of candidate events, and presents an analysis of our uniquely identified candidate and its inferred source parameters, as well as a discussion of areas for improvement in our search pipeline going forward.

II. METHOD

Our search method produces triggers using matched filtering, followed by a deep learning model that makes predictions on the SNR time series of these triggers. The ranking statistic is derived from these predictions and used to assign significance to a trigger. Matched filtering is the cross-correlation of detector strain data with a template waveform to produce a signal-to-noise ratio

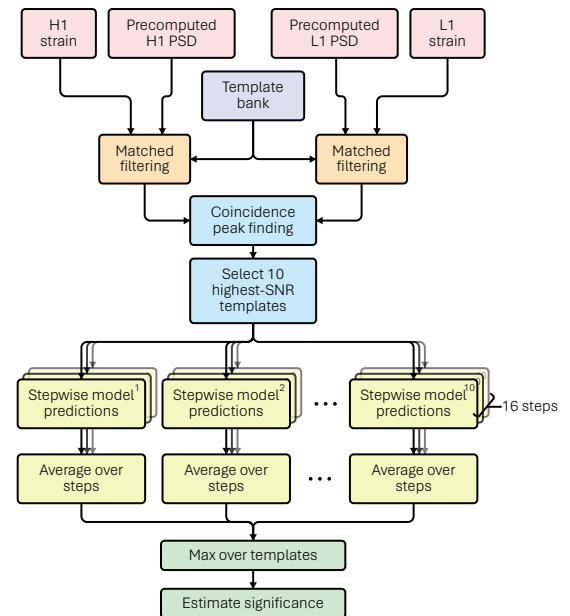


FIG. 1. A flowchart of the search pipeline presented in this paper. The pipeline takes in public O3 data from the LIGO-Hanford (H1) and LIGO-Livingston (L1) detectors, as well as pre-computed PSDs of this data (Sec. II A). The data is downsampled to 2048 Hz, and we perform matched filtering using a BBH template bank (Sec. II B). A peak-finding algorithm then produces triggers based on SNR > 4 peaks in at least one detector in the SNR time series, and identifies a coincident peak in the other detector within the light-travel time between detectors (~ 10 ms). For each second of analyzed data, triggers are generated from the 10 highest network SNR templates, and the SNR time series is sent to our pre-trained deep learning model (Sec. II C and Sec. II D) for predictions. We perform 16 predictions by stepping through the SNR time series in increments of $1/16$ th of a second for each trigger. These stepwise predictions start when the trigger time first enters the deep learning model’s 1-second viewing window and continue until it exits the window; the average of these predictions is then taken. We retain one of the 10 template triggers per second that has the highest average model prediction, and this quantity becomes the search pipeline’s ranking statistic. The false alarm rate and probability of astrophysical origin can be estimated (Sec. II E) by comparing the ranking statistic to empirical results from our search pipeline’s analyses on time-shifted data and injections.

time series. In practice, an extensive collection of waveforms, known as a template bank, is used to search across the parameter space of compact binary objects. We have built a search pipeline that computes the SNR time series for our entire template bank, applies a template selection criterion using a peak-finding algorithm, and then uses a deep learning model to make predictions on the SNR time series and produce a ranking statistic and significance estimates. Figure 1 presents a flowchart of our search pipeline.

Section II A discusses the available data from the O3 observing run that we use for all training and analyses presented in this work. We discuss our chosen template bank in Section II B. In Section II C, we discuss how we constructed the training dataset for our deep-learning model to achieve high sensitivity across the BBH parameter space. We discuss the implementation details of our deep-learning model further in Section II D. Lastly, we discuss how we compute our false alarm rate and probability of astrophysical origin metrics using our ranking statistic in Section II E.

A. Data

We use public data from O3 [59] for the Hanford and Livingston LIGO detectors, sampled at 2048 Hz, for the model training and analyses presented herein. The O3 observing run consists of two distinct periods with a break in the middle for detector upgrades. The first period is O3a, running between 1 April 2019 15:00 UTC and 1 October 2019 15:00 UTC, and the second period is O3b, running from 1 November 2019 15:00 UTC to 27 March 2020 17:00 UTC. We require that both LIGO detectors have coincident data available and that each data segment have a minimum duration of 1024 seconds. This results in 106.2 days of data in O3a and 96.0 days in O3b. We do not use data from the Virgo detector due to its comparatively low sensitivity [8].

For our offline search, we process the data in chunks of 1024 seconds. We perform matched filtering with a low frequency cutoff of 15 Hz and do not produce triggers in the first 200 s of each analysis segment to avoid filter wraparound effects for the longest waveforms in the template bank [60]. We also do not produce triggers in the final 24 s of each analysis segment to account for edge effects from whitening with the power spectral density (PSD). These cuts reduce our livetime for sensitivity tests and offline search to 104.6 days in O3a and 94.7 days in O3b.

To maintain consistency in our analyses and account for changes in PSDs over time, we aggregate data by calendar weeks of the O3 timeline. We compute the PSDs for matched filtering over the entire week of analyzed data. No data is available between weeks 27 and 31 due to the break between O3a and O3b. Additionally, weeks 27, 31, and 52 have reduced observing time because the observing runs do not start or end on calendar-week boundaries.

B. Template bank

The template bank used for this work is a subset of the templates from GstLAL’s second observing run template bank [61], serving as a simple starting point for our search pipeline. The SPIIR pipeline also used this template bank for the real-time search during O3 [62]. We use

a subset of the template bank in which both component masses exceed $2 M_{\odot}$, yielding 97,802 templates. This parameter space for our BBH search is selected based on the population of injections defined in the GWTC-3 BBH set of injections [8, 63]. We use the SEOBNRv4_ROM waveform approximant [64] with $f_{\text{low}} = 15$ Hz for our matched-filter template waveforms.

C. Training dataset

The training dataset balances SNR time series samples of pure noise, glitch-contaminated noise, and injected BBH signals to expose the deep-learning model to realistic noise backgrounds and signals. We use strain data from week 1 of the O3 observing run for the noise background. We pair data from each detector by offsetting the strain in time by an interval longer than the light travel time between the detectors (~ 10 ms), ensuring the model never sees coincident detector data during training. The strain data and subsequent SNR time series have a sampling rate of 2048 Hz, and the training sample length is one second.

The background noise exhibits non-stationary, non-Gaussian behaviour. Of this behavior, the primary concern is the occurrence of frequent, short-duration glitches that can lead to false triggers in search pipelines [65, 66]. For this work, we use the existing Omicron software package [67] to identify transient noise events, enabling us to select data segments with and without glitches for use in our training dataset. During training, we only consider glitches identified by Omicron with an SNR greater than 6. Following the method in Ref. [58], injected signals are placed relative to glitches such that the frequency content of the glitch aligns with the corresponding frequency in the injected waveform, ensuring that the glitch and the signal contribute to the matched filter SNR at the same time, maximizing their interaction. To prevent the glitch from always appearing centered in the SNR time series, we apply a random temporal shift of up to ± 0.5 seconds to the injected signal’s position. Compared to our past work, we increase the proportion of samples containing glitches to 30% to both improve model behavior in the presence of glitches and account for the random timing of glitches.

The training dataset contains 100,000 strain samples with only noise and 100,000 strain samples with injected BBH signals added to the noise. During training, we reserve 20% of these samples for validation. As discussed previously, we pair each strain sample with 10 templates, with template selection governed by distinct strategies for noise-only and injection samples. Noise-only samples use randomly chosen templates, with each template having an equal chance. For injection samples, a set of 500 templates is initially selected by sorting the template bank by chirp mass, and taking 250 templates from either side of the injection’s chirp mass. The match — the maximized overlap — is then calculated for each template using the

injection waveform. Finally, the highest-matching template and nine others, randomly selected with a match greater than 0.5, are chosen to produce the training samples with injected signals.

For the set of injected signals, we optimize the parameter distributions to most effectively train our model to detect signals across the parameter space we search. In Ref. [57], we found that using astrophysical priors for all injected signal parameters in the training dataset resulted in low sensitivity at higher masses, due to the astrophysical distribution being sharply biased toward low masses and containing very few samples at higher masses. We counteract this by manually controlling the density of injections in the source frame chirp mass. We choose source frame component masses to be between 2 and $100 M_{\odot}$, meaning the chirp mass has a lower bound corresponding to a $2\text{-}2 M_{\odot}$ pair and an upper bound of a $100\text{-}100 M_{\odot}$ pair. This range is chosen based on the selected astrophysical parameter space for binary black hole mergers in the LVK’s GWTC-3 catalog [8, 63], despite the low-mass region being more likely to represent mergers containing one or more neutron stars. To control the distribution of injections in chirp mass, we sample $\mathcal{O}(10^7)$ injections from astrophysical priors matching those in the GWTC-3 injection set [63]. From this large set of injections, we divide the source-frame chirp mass space into 50 bins, and each bin randomly samples events from the more extensive set in that region. The chosen chirp mass distribution is linear and decreasing, with twice as many events in the lowest chirp mass region as in the highest, as shown in Figure 2. Following this sampling, we adjust the luminosity distances of each sample to achieve a desired expected network SNR, ensuring the distribution follows a power law with an exponent of -3, with lower and upper bounds of 6 and 1000. Here, expected SNR refers to the optimal matched-filter SNRs for a simulated signal. The resulting dataset preserves astrophysical distributions for the intrinsic and extrinsic parameters unrelated to masses and distances.

Injection waveforms are generated using the SEOB-NRv4PHM model [68], or the SEOBNRv4P model [68] if the binary has a detector frame total mass below $9 M_{\odot}$, as in GWTC-3 [8]. Higher-order modes are excluded at these lower masses because they would lie above the Nyquist frequency of the strain data. We position injection merger times so they fall within the central 0.9 seconds of the resulting 1-second SNR training sample, thereby training the model to identify signals across its input window.

D. Model implementation

The model is constructed and trained using TENSORFLOW [69], and the model architecture is the same as was used in Ref. [57]. The model takes as input the SNR time series from both detectors and consists of a series of convolutional [70], residual (ResNet) [71], and fully

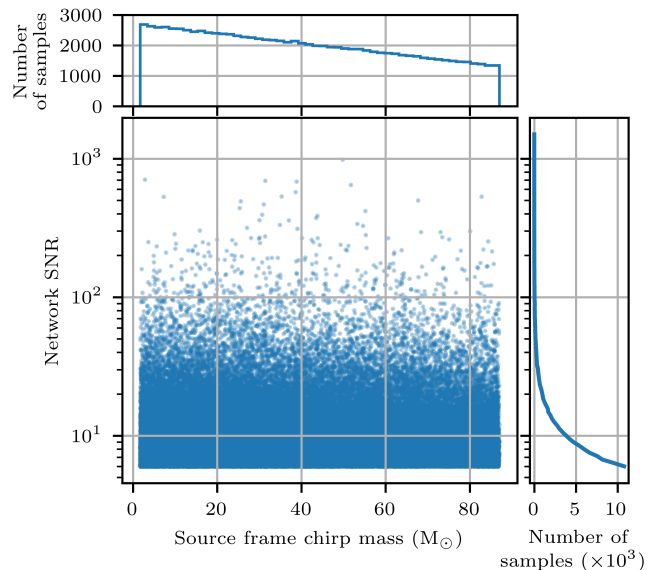


FIG. 2. Source frame chirp mass and network signal-to-noise ratio (SNR) parameter distributions for the training dataset injection samples. The top histogram illustrates the bias towards low-mass signals, with twice as many samples in the lowest mass bin as in the highest mass bin. The right histogram shows the power-law distribution of network SNR. We chose these distributions to account for low injection counts in the high-mass and high-SNR regions when sampling from an astrophysical distribution.

connected layers that process each detector’s data separately before combining them to form a single model output. During training, the model employs a sigmoid activation function on the output to constrain it to 0-1, enabling the use of the binary cross-entropy loss function and accuracy as training metrics. Our model employs 32-bit floating-point precision and is susceptible to numerical overflow and underflow (rounding to 1 or 0). As a result, we remove the sigmoid activation function after training, resulting in an unbounded output that we use to compute the ranking statistic for our search.

After training the model and removing the sigmoid function on the model output, we accelerate its inference by converting it to an ONNX model with ONNX RUNTIME [72]. Using ONNX allows us to run our offline search without a GPU, as CPU-based predictions are efficient enough to keep up with the other search pipeline components, and CPUs were more accessible than GPUs at the time of the analyses presented in this work.

E. Search statistics

As mentioned at the start of Section II, our search pipeline’s ranking statistic is the highest average prediction from our deep-learning model on the SNR time series from the ten templates with the highest SNR over a given

second, limiting our trigger rate to one per second. The purpose of the ranking statistic is to assign significance to a trigger, thereby classifying it as arising from noise or a gravitational wave signal based on a specific threshold. Gravitational wave detection uses two main statistics for classification: the false alarm rate (FAR) and the probability of astrophysical origin (p_{astro}).

1. False alarm rate

The false alarm rate (FAR) is an approximate measure of how often a search would produce a trigger, assuming it were caused by noise, with a specific value of the ranking statistic, \mathcal{R} . We compute the FAR by collecting a background distribution of the ranking statistic and examining the rate at which these noise triggers occur; this allows us to assign an FAR to future triggers produced by the search. Currently, the false alarm rate is used as the public alert threshold for significant compact binary coalescence events during LVK observing runs, with any triggers with an FAR below 1 per month released to the public during O4 [73].

To scale up the amount of available background data, we decouple the strain from each detector by shifting them in time by an amount greater than the light travel time between the detectors. This shift results in a noise dataset with no coincident astrophysical events, but non-stationary noise artifacts remain, so that it can be treated as pure noise by most searches. Additionally, applying these shifts multiple times to the same strain segments multiplies the available noise data, meaning relatively little data is needed to surpass the FAR thresholds commonly used for public alerts. When collecting background, we shift the noise background data 100 times by increments greater than the light travel time, to achieve ~ 1.5 years of collected background data from one week of O3 data.

Since our search produces triggers when at least one detector has an SNR greater than 4, we remove times of strain from the noise background that include candidate events in the GWTC-3 catalog to avoid contaminating the background. When analyzing our pipeline's performance, we identified drift in the distribution of the ranking statistic over time, so we regularly update our background collection as follows. At the start of O3a, we collect background on weeks 2 and 3, since we trained on week 1, and each has less Hanford-Livingston coincident data than desired. For the start of O3b, we use weeks 31 and 32, where week 31 is the beginning of O3b but has less strain than desired to collect enough background. Our background data is then updated at regular intervals on weeks 5, 9, 13, 17, 21, and 25 in O3a, and on weeks 35, 39, 43, 47, and 51 in O3b. We use the updated background data to assign FARs in the same week it is collected, and every week until the following week that we collect new background data.

Due to the limited quantity of collected background

each time we update it, we fit a linear function to the tail of the background data and use this to assign continuous FAR values below 1 per 2 months. We compute the fitted line as the weighted average of 10 fits from 10 random, independent subsets of the collected background. The coefficient of determination, R^2 , of each fit weights the slope and offset components to compute the overall fit.

2. Probability of astrophysical origin

While the false alarm rate gives us a measure of the expected rate of a trigger if it were to come from noise, it does not provide a direct measure of how likely a candidate trigger is to originate from an astrophysical source. The probability of astrophysical origin, p_{astro} , estimates the probability that a candidate trigger represents a real gravitational wave signal. In contrast to the false alarm rate, the probability of astrophysical origin incorporates knowledge of the astrophysical signal rate and population.

The original method for computing p_{astro} is the FGMC method [74]. It constructs a two-component model that assumes only two event types exist: noise (background) and signal (foreground). If we consider only triggers above a threshold where the background dominates the population of triggers, we can model the foreground and background trigger rates as two independent Poisson processes. For this, we consider triggers below an FAR threshold of 1×10^{-4} Hz. Since we treat our pipeline as only searching for binary black hole mergers, we do not introduce additional complexity into the model by computing the p_{astro} for multiple source types. We also tune separate p_{astro} models for the O3a and O3b observing runs; however, the tuning method is identical.

Our p_{astro} implementation is based on the implementation provided by the LVK's P-ASTRO⁴ package, and is the same method the SPIIR pipeline [62] uses to produce p_{astro} estimates for real-time detections as of the time of writing. To compute the p_{astro} , we use a signal-versus-noise Bayes factor, defined as the ratio of analytically estimated foreground and background likelihood distributions. Given a set of N candidate events $\vec{x}_N = \{x_0, x_1, \dots, x_{N-1}\}$, we can compute the mean values for the background Poisson count, $\langle \Lambda_0 \rangle_N$, and the foreground Poisson count, $\langle \Lambda_1 \rangle_N$. The probability of astrophysical origin of a new candidate, x_{N+1} , is [75]:

$$P_1(x_{N+1} | \vec{x}_{N+1}) = \frac{\langle \Lambda_1 \rangle_N K(x_{N+1})}{\langle \Lambda_0 \rangle_N + \langle \Lambda_1 \rangle_N K(x_{N+1})}, \quad (1)$$

where x are the ranking statistics associated with a candidate, and $K(x)$ is the signal-versus-noise Bayes factor.

Following the approach in GWCELERY, we model the background density distribution, $p_0(\mathcal{R})$, in terms of the

⁴ <https://git.ligo.org/lscsoft/p-astro>

ranking statistic \mathcal{R} , as the fraction of background events below an FAR threshold value that will have a specified FAR. This can be written in terms of false alarm rate, \mathcal{F} ,

$$p_0(\mathcal{R}) = \frac{\mathcal{F}(\mathcal{R})}{\mathcal{F}_{\text{th}}}, \quad (2)$$

where we express the false alarm rate as a function of the ranking statistic and the threshold FAR, \mathcal{F}_{th} , is a value that has to be tuned. The foreground distribution, $p_1(\rho)$, represents the likelihood that a signal is observed with an SNR ρ , given that a signal is detected above an SNR threshold ρ_{th} . Assuming a distribution of sources that is uniform in volume, the foreground distribution is [76–78]:

$$p_1(\rho) = \frac{3\rho_{\text{th}}^3}{\rho^4}, \quad (3)$$

where ρ_{th} is a threshold SNR value that has to be tuned. From these analytic estimates, the Bayes factor, $K(\rho, \mathcal{R})$ can be defined as,

$$\begin{aligned} K(\rho, \mathcal{R}) &= \frac{p_1(\rho)}{p_0(\mathcal{R})} \\ &= \frac{3\rho_{\text{th}}^3 \mathcal{F}_{\text{th}}}{\rho^4 \mathcal{F}(\mathcal{R})}, \end{aligned} \quad (4)$$

In principle, a probability of astrophysical origin of 0.5 should indicate a trigger at a ranking statistic value where the trigger densities of background and foreground triggers are equal. This feature is how we tune the values of ρ_{th} and \mathcal{F}_{th} , using empirical trigger densities of the background and foreground. Here, the background empirical distribution combines all background points from time-shifted triggers for a given observing run, as outlined in Section II E 1. We estimate the foreground empirical distribution from the triggers produced in the first three weeks of injection run testing in each half of the O3 observing run, and the specific weeks are outlined in Section III. Figure 3 presents these trigger density distributions from O3a as a function of the false alarm rate. We tune the ρ_{th} and \mathcal{F}_{th} in the p_{astro} model such that for a test dataset of injection run results, the FAR value where the trigger densities intersect approximately lines up with a p_{astro} of 0.5, as can be seen in Figure 4. Figure 4 represents the case in O3a, where the injections used are from weeks 18 and 20 using the GWTC-3 binary black hole injection set [63]. Significant deviations from the S-curve in Fig. 4 mainly occur when injections have low likelihood in the deep learning model training data set or the astrophysical BBH population used to tune the p_{astro} model. These cases - typically injections with high component masses or masses consistent with an NSBH source - result in a less well-constrained relationship between FAR and SNR, yielding uncertain p_{astro} values. For tuning the O3b p_{astro} , we test the model on injections from weeks 48 and 50. The tuned values for $\{\rho_{\text{th}}, \mathcal{F}_{\text{th}}\}$ are $\{8.5, 10^{-4}\}$ for O3a, and $\{7.25, 10^{-4}\}$ for O3b.

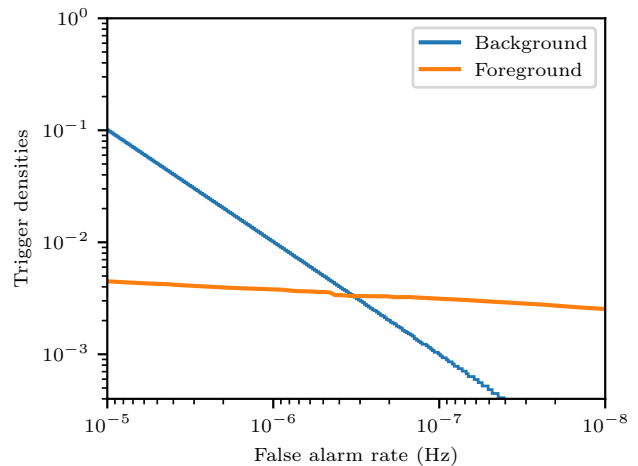


FIG. 3. Foreground (orange) and background (blue) trigger density distribution for our search pipeline in O3a. We tune our p_{astro} model such that the FAR at the intersection of the two distributions corresponds to a p_{astro} of 0.5.

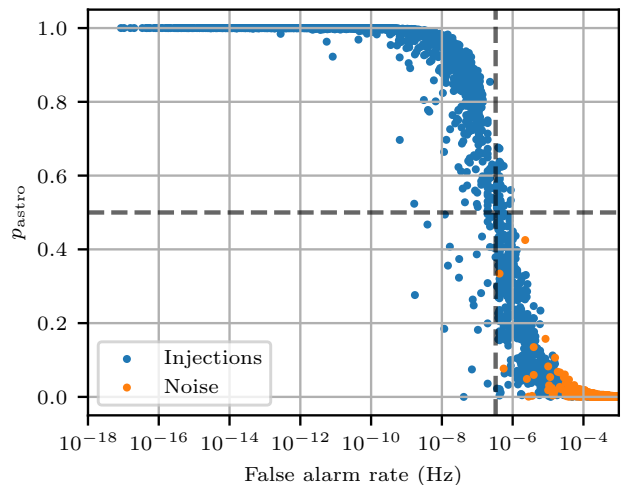


FIG. 4. Probability of astrophysical origin (p_{astro}) results on injection runs in weeks 18 and 20 of O3. We observe that a p_{astro} of 0.5 (horizontal black dotted line) correlates roughly to the cross-over FAR from Figure 3 (vertical black dotted line).

III. SEARCH SENSITIVITY

To compare our search pipeline with existing pipelines, we quantify search sensitivity in terms of the spacetime volume in which signals can be detected - the sensitive hypervolume $\langle VT \rangle$ - using injected gravitational wave signals throughout the O3 observing run. The set of injected signals we use is from the BBH-only injection sets provided by the LVK with the third gravitational wave transient catalog [63]. Using this dataset enables us to compare the sensitivity of our search with that of the exist-

ing cWB, GstLAL, MBTA, PyCBC-broad and PyCBC-BBH searches, as the p_{astro} and FAR results from these searches are provided. We treat the PyCBC-broad and PyCBC-BBH pipelines as independent; however, they differ only in the template bank parameter space (BNS, NSBH, and BBH versus just BBH), and the PyCBC-BBH pipeline ranking statistic incorporates a chirp mass weighting for triggers [8, 25]. The sensitivity comparisons we present serve only as a general benchmark, as each search pipeline is developed with a different search space and tuned towards sensitivities in various areas of the shared parameter space.

For this work, we search for injected signals every other week, starting in week 4 in O3a and in week 32 in O3b. The result is 83,815 binary black hole signal injections. Other searches look for injections during other weeks and through different online detector configurations, which would increase their sensitive hypervolume. Additionally, each search pipeline has its own template bank, each with varying parameter spaces. However, for this work, we consider only the sensitivity of the other searches to the same BBH injections we are searching for, aiming for a more direct comparison of sensitivity before developing single-detector search capabilities and two- and three-detector searches involving Virgo. Extending our search to detect events across the full BNS and NSBH parameter spaces is expected to reduce sensitivity in the BBH region, thereby changing the population of noise events produced by our search.

The calculation of the sensitive hypervolume is described in Refs. [8, 63], where it quantifies the sensitivity of a search to a population of sources uniformly distributed in comoving volume and source-frame time. The expected number of detections, \hat{N} , for a search is [8]

$$\hat{N} = \langle VT \rangle R, \quad (5)$$

where R is the rate of signals per unit volume per unit observing time. The thresholds we use to compute sensitivity results are $p_{\text{astro}} \geq 0.5$ and an FAR of less than 2 per day. For our search, we assign to an injection the most significant trigger within ± 1 seconds of the merger time. We compute the sensitive hypervolume for the mass combinations used in the GWTC-3 paper [8], together with three additional mass pairs with a primary mass of $50 M_{\odot}$, to parametrize the sensitivity across the parameter space and to observe trends in sensitive regions for each search.

In Table I, we report the sensitive hypervolume at each mass combination used to parametrize the search space. Figure 5 shows the variation in the sensitive hypervolume between each search across the BBH parameter space. To calculate the sensitive hypervolume around each mass pair, injections are weighted so that they follow a log-normal distribution around the central mass with a standard deviation of $0.1 M_{\odot}$, and we assume that the component spins are isotropically distributed with uniformly distributed magnitudes [8]. In addition to computing the sensitivity of each search included in the GWTC-3 paper,

we calculate combined sensitivity metrics with and without our search pipeline to assess the impact of our search on combined detection efforts.

Relative to PyCBC-BBH, our search is less sensitive overall. Among the all-source pipelines (GstLAL, MBTA, PyCBC-broad), our search pipeline is comparable at higher masses but degrades for signals at or below a source-frame chirp mass of $\sim 25 M_{\odot}$ and an expected network SNR of ~ 15 . This low-mass sensitivity gap does not imply an intrinsic limitation of the method, as we have shown in past work that we can detect BNS signals [58]. Instead, it likely reflects that the training dataset and configuration choices did not optimize sensitivity over the vast BBH space.

For mass pairs with a $50 M_{\odot}$ primary component, our sensitivity appears to drop as the mass ratio, q , decreases relative to other searches; however, the size of our injection set prevents us from independently investigating mass-ratio effects and overall low-mass sensitivity.

Including our search increases the combined sensitive hypervolume, notably from the $20\text{-}20 M_{\odot}$ bin and above (Table I). As expected, our contribution to the combined sensitive volume decreases at lower masses, where our sensitivity is lower.

Table II provides the total number of detections from each search pipeline during the O3 observing run, as well as the count of unique detections for each pipeline in the combined detection scenarios, both with and without our search pipeline included. GWTC-3 [8] requires that injections detected by cWB are also detected by another search, but we do not impose that criterion here. Our search yields the most unique detections among the overall population of injected signals. The following section, Section III A, demonstrates that this significant result is a feature of our deep-learning ranking statistic approach.

A. Comparison with a BBH-only PyCBC search

To determine whether the significant, unique contributions of our search are due to the template bank or to our ranking statistic, we ran the PyCBC search pipeline using our template bank over weeks 4, 6, and 8 and compared the detected signal populations. Here, we are using the PyCBC-broad version of the pipeline, which does not include weighting higher-chirp-mass triggers, as the PyCBC-BBH pipeline does.

Because estimates of p_{astro} were not available in the PyCBC configuration we used, we set a detection threshold of $\text{FAR} < 2$ per month for both pipelines, consistent with the open public alert threshold used for real-time detections in O3 [8]. The change from using p_{astro} as a detection threshold to using FAR is not a concern, as we find that the injection recovery rates are consistent with the counts observed in Table II.

There are 10,472 total injections in the set analyzed by PyCBC using our bank, and the detection counts for each search using FAR as the threshold are shown in Table III.

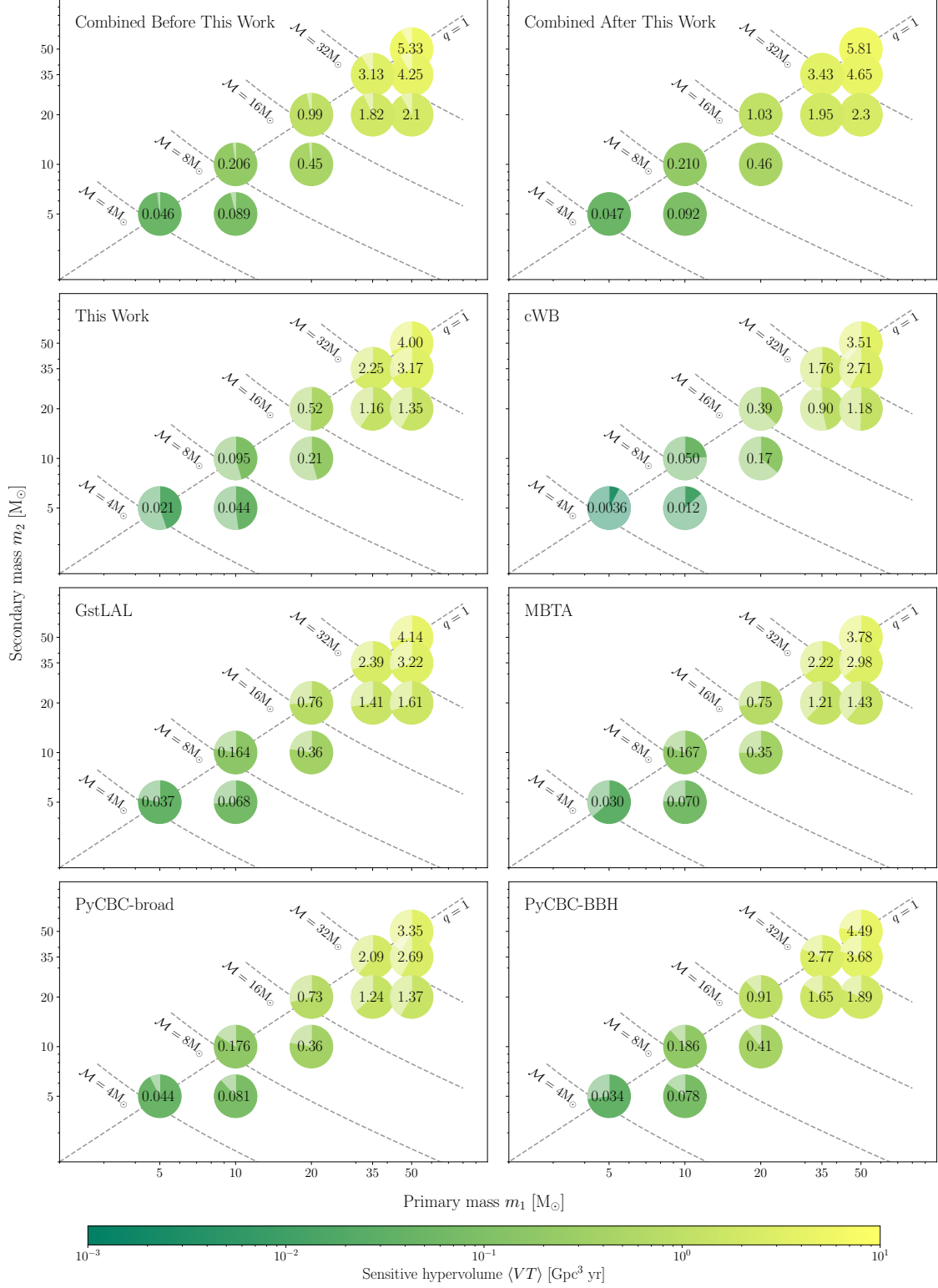


FIG. 5. Sensitive hypervolume, $\langle VT \rangle$, from the O3 observing run for our search pipeline and the searches presented in GWTC-3 [8]. Additionally, we include two $\langle VT \rangle$ estimates for injections identified by at least one search pipeline, both before and after considering our own search pipeline, to demonstrate the significant, unique contributions of our analysis. The detection threshold is $p_{\text{astro}} \geq 0.5$ and $\text{FAR} < 2$ per day, and we compute the sensitive hypervolume at component mass pairs that act as the central point of a log-normal distribution with a standard deviation of $0.1 M_\odot$. Each $\langle VT \rangle$ estimate is marked with a pie chart where the darker region indicates the fraction of the combined $\langle VT \rangle$ that is recovered. The color of the darker region of each point is defined by the value of the $\langle VT \rangle$, as given by the color scale. The $\langle VT \rangle$ values and mass pairs are the same as those given in Table I.

m_1, m_2	Sensitive hypervolume (Gpc ³ yr)							
	cWB	GstLAL	MBTA	PyCBC-broad	PyCBC-BBH	This Work	Combined*	Combined [†]
50, 50	$3.51^{+0.08}_{-0.07}$	$4.14^{+0.09}_{-0.08}$	$3.78^{+0.08}_{-0.08}$	$3.35^{+0.07}_{-0.08}$	$4.49^{+0.09}_{-0.08}$	$4.00^{+0.08}_{-0.09}$	$5.33^{+0.09}_{-0.10}$	$5.81^{+0.09}_{-0.10}$
50, 35	$2.71^{+0.07}_{-0.06}$	$3.22^{+0.07}_{-0.07}$	$2.98^{+0.06}_{-0.07}$	$2.69^{+0.07}_{-0.06}$	$3.68^{+0.07}_{-0.08}$	$3.17^{+0.07}_{-0.07}$	$4.25^{+0.08}_{-0.08}$	$4.65^{+0.08}_{-0.09}$
50, 20	$1.18^{+0.07}_{-0.08}$	$1.61^{+0.09}_{-0.09}$	$1.43^{+0.08}_{-0.09}$	$1.37^{+0.08}_{-0.09}$	$1.89^{+0.10}_{-0.09}$	$1.35^{+0.08}_{-0.08}$	$2.14^{+0.11}_{-0.10}$	$2.34^{+0.10}_{-0.11}$
35, 35	$1.76^{+0.04}_{-0.04}$	$2.39^{+0.05}_{-0.05}$	$2.22^{+0.05}_{-0.04}$	$2.09^{+0.05}_{-0.05}$	$2.77^{+0.06}_{-0.05}$	$2.25^{+0.05}_{-0.05}$	$3.13^{+0.06}_{-0.06}$	$3.43^{+0.06}_{-0.07}$
35, 20	$0.90^{+0.04}_{-0.04}$	$1.41^{+0.05}_{-0.05}$	$1.21^{+0.05}_{-0.04}$	$1.24^{+0.05}_{-0.04}$	$1.65^{+0.05}_{-0.05}$	$1.16^{+0.04}_{-0.04}$	$1.82^{+0.05}_{-0.06}$	$1.95^{+0.06}_{-0.05}$
20, 20	$0.39^{+0.01}_{-0.02}$	$0.76^{+0.02}_{-0.02}$	$0.75^{+0.02}_{-0.02}$	$0.73^{+0.02}_{-0.02}$	$0.91^{+0.02}_{-0.03}$	$0.52^{+0.02}_{-0.02}$	$0.99^{+0.03}_{-0.02}$	$1.03^{+0.02}_{-0.02}$
20, 10	$0.17^{+0.01}_{-0.02}$	$0.36^{+0.02}_{-0.02}$	$0.35^{+0.01}_{-0.02}$	$0.36^{+0.02}_{-0.02}$	$0.41^{+0.02}_{-0.02}$	$0.21^{+0.02}_{-0.01}$	$0.45^{+0.03}_{-0.02}$	$0.46^{+0.02}_{-0.02}$
10, 10	$5.0^{+0.4}_{-0.4} \times 10^{-2}$	$0.16^{+0.01}_{-0.01}$	$0.17^{+0.01}_{-0.01}$	$0.18^{+0.01}_{-0.01}$	$0.19^{+0.01}_{-0.01}$	$9.5^{+0.5}_{-0.5} \times 10^{-2}$	$0.21^{+0.01}_{-0.01}$	$0.21^{+0.01}_{-0.01}$
10, 5	$1.2^{+0.3}_{-0.2} \times 10^{-2}$	$6.8^{+0.6}_{-0.5} \times 10^{-2}$	$7.0^{+0.6}_{-0.6} \times 10^{-2}$	$8.1^{+0.6}_{-0.6} \times 10^{-2}$	$7.8^{+0.6}_{-0.6} \times 10^{-2}$	$4.4^{+0.5}_{-0.4} \times 10^{-2}$	$8.9^{+0.6}_{-0.6} \times 10^{-2}$	$9.2^{+0.6}_{-0.6} \times 10^{-2}$
5, 5	$3.6^{+0.6}_{-0.6} \times 10^{-3}$	$3.7^{+0.2}_{-0.2} \times 10^{-2}$	$3.0^{+0.2}_{-0.2} \times 10^{-2}$	$4.4^{+0.2}_{-0.2} \times 10^{-2}$	$3.4^{+0.2}_{-0.2} \times 10^{-2}$	$2.1^{+0.1}_{-0.1} \times 10^{-2}$	$4.6^{+0.2}_{-0.2} \times 10^{-2}$	$4.7^{+0.2}_{-0.2} \times 10^{-2}$

TABLE I. Search pipeline sensitive hypervolumes for different mass combinations, using a probability of astrophysical origin greater than or equal to 0.5 and a false alarm rate less than 2 per day as the detection threshold. The combined columns refer to the combined sensitive hypervolume, requiring that at least one search pipeline detects a given event. The asterisk (*) refers to the combination of the cWB, GstLAL, MBTA, PyCBC-broad, and PyCBC-BBH searches, and the dagger (†) refers to the combined sensitivity after including our search in this list.

	cWB	GstLAL	MBTA	PyCBC-broad	PyCBC-BBH	This Work
Total	18,118	29,303	27,060	26,589	31,392	23,238
Unique*	1,000	1,155	1,796	270	2,460	-
Unique [†]	684	946	1,370	236	2,043	2,612

TABLE II. Total counts of detected injections in O3 for each search pipeline (top row) and the number of uniquely detected events for each search pipeline before (*) and after (†), including the results of our search pipeline (bottom two rows). The detection threshold used is a probability of astrophysical origin greater than or equal to 0.5 and a false alarm rate less than 2 per day. These results demonstrate the significant and unique detection contributions of our work, as well as our support for detecting events previously identified by a single search pipeline.

We observe that the PyCBC ranking statistic identifies more injections than our search, as expected given our low total sensitivity. Despite this, the number of uniquely detected events in the combined detections configuration for our search pipeline (348) is significantly higher than PyCBC using our bank (23), indicating that our deep-learning ranking statistic is the reason we can detect a unique population of signals, rather than the choice of template bank. Based on this finding, the large number of uniquely identified events in our search, outlined in Table II, is due to our unique search method rather than our choice of template bank.

Figure 6 demonstrates that the difference in total detection counts between our search pipeline and PyCBC with our template bank is due to our lack of sensitivity at low masses. Conversely, when directly comparing the populations of detected events using only our search pipeline and PyCBC with our template bank, our search identifies 726 unique events. The distribution of source-frame chirp masses for our search’s 726 uniquely detected

events is also plotted in Fig. 6. This distribution closely matches that of all detected events, suggesting that an increase in sensitivity at lower masses will likely yield even more uniquely detected events; however, this is not guaranteed. Large unique detection counts further suggest that, despite detecting a consistent number of events at higher chirp masses, the search pipelines are not detecting the same events, which may become very important when conducting searches for real gravitational wave signals.

B. Sensitivity over time

Since we need to train a deep learning model for our search, it is essential to determine how often the model will need to be retrained due to drift in the detector sensitivity. It is also necessary to consider the change in search sensitivity due to the instrument upgrades performed between O3a and O3b [79].

	cWB	GstLAL	MBTA	PyCBC-broad	PyCBC-BBH	This Work	PyCBC-Our Bank
Total	2,427	3,835	3,271	3,122	3,751	2,916	3,369
Unique*	75	188	183	28	249	-	-
Unique [†]	66	164	129	26	207	348	-
Unique [‡]	67	179	180	15	211	-	23

TABLE III. Total count of detected injections for each search pipeline in weeks 4, 6 and 8 of the third observing run (top row). Number of uniquely detected events per search pipeline in three different combinations of searches: the five GWTC-3 search pipelines (*), the five GWTC-3 search pipelines plus this work ([†]), and the five GWTC-3 search pipelines plus PyCBC-Our Bank ([‡]). The PyCBC-Our Bank column refers to our PyCBC analysis using the template bank used by our search pipeline. The detection threshold used here is a false alarm rate of less than 1 per 2 months. The larger quantity of unique detections from our work compared to PyCBC-Our Bank demonstrates that our work’s unique detection ability stems from our deep-learning ranking statistic rather than the template bank.

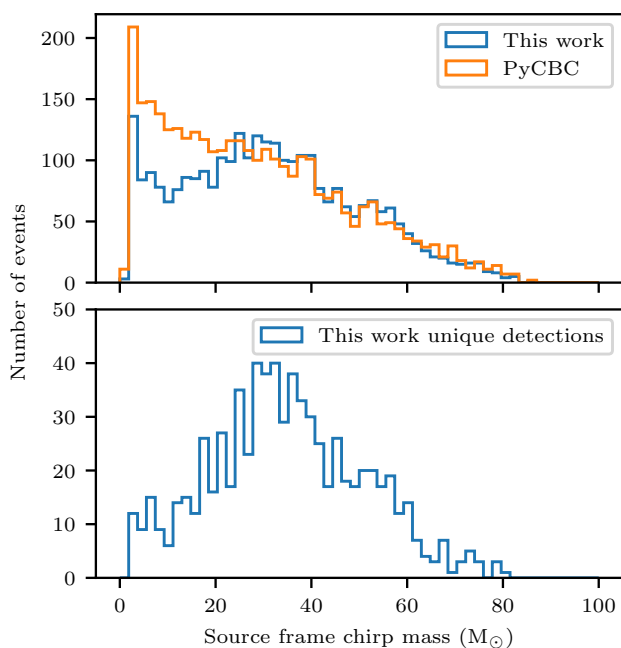


FIG. 6. Comparison of detected injection counts over source-frame chirp mass between PyCBC (run using our template bank) and our search pipeline, for injections in weeks 4, 6, and 8 of the O3 observing run (top). Distribution of events detected by our search pipeline and not detected by PyCBC with our template bank (bottom).

To visualize how our model’s sensitivity changes over time, we compute the fraction of detected signals for each injection run week we analyze. Figure 7 presents the fraction of signals detected with $p_{\text{astro}} \geq 0.5$ and FAR < 2 per day for each pipeline and the combined detection scenarios before and after including our search pipeline. We use the fraction of recovered events as the metric, as in Ref. [54], to separate the detector sensitivity from the search-pipeline sensitivities. We observe no significant or consistent change in sensitivity over time and note

that our results follow the general trends in sensitivity observed during the O3 observing run.

Going from O3a to O3b, there appears to be a drop in sensitivity for our search relative to other searches, as well as a drop in the increase between the combined detection configurations. We look at this further in Figure 8, where we observe a significant decrease between O3a and O3b in the ratio of total detected events before and after including our search in the combined detection configurations. However, the minimum increase in the number of detected events by including our search is only 4.74 %, which remains a significant addition. The large spread in Fig. 8 makes it challenging to verify the sensitivity to unique events over time; however, training our deep-learning model on real noise from more extended periods throughout O3 is expected to stabilise the sensitivity.

From these results, it is clear that retraining would not be necessary on a weekly or monthly time scale with our current training setup. We could use noise from a more extended period to train the model, rather than only the first week of O3, to reduce variation in the model’s sensitivity over time. Other deep-learning gravitational wave searches have demonstrated satisfactory performance with longer training time scales [53, 80]. Our decrease in unique detection counts between O3a and O3b suggests that retraining between observing runs, when detector upgrades are performed, is important for improving our search performance over time.

IV. OFFLINE SEARCH

In this section, we conduct an offline search for BBH gravitational wave signals in O3 data. We present the results of this search in terms of candidate events identified by our search pipeline, as well as those candidates that we do not identify, which have been identified by previous existing offline searches. These previous offline searches include the GWTC [6–8], OGC [26, 27], IAS [41–43], PyCBC-KDE [38], cWB [47], AresGW [53]

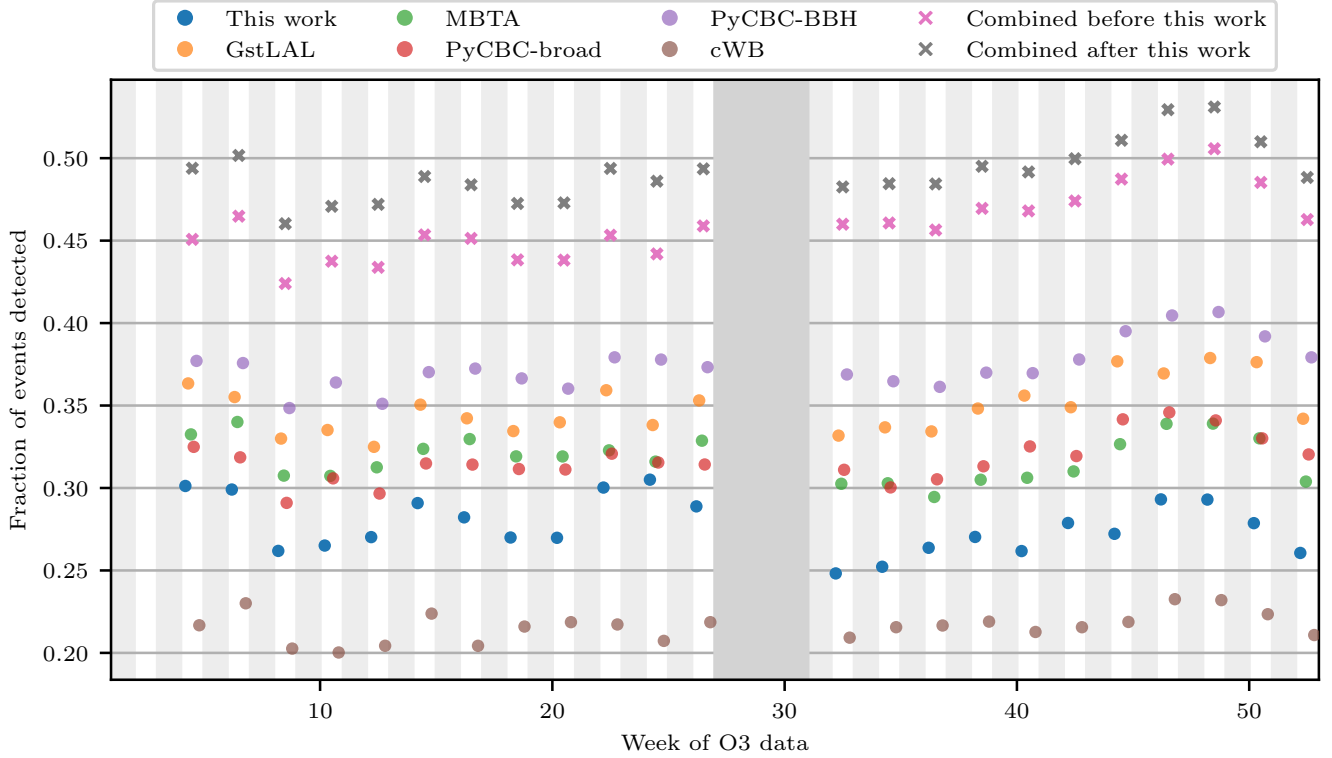


FIG. 7. Search sensitivities in terms of the fraction of detected events over the course of the O3 observing run. The detection threshold for each search pipeline is a probability of astrophysical origin greater than or equal to 0.5 and a false alarm rate less than 2 per day. The combined sensitivity metrics (crosses) refer to the scenario where at least one search pipeline detects an event, both before and after our search pipeline is included. These combined sensitivity metrics demonstrate the impact of the unique detections made by our search pipeline and that our sensitivity is consistent over time.

and Aframe [55] catalogs. The OGC, IAS, and PyCBC-KDE catalogs are produced using matched-filter searches; cWB is an unmodeled burst-search pipeline; and AresGW and Aframe are deep-learning searches that identify candidates from detector strain data.

With a candidate identification threshold of $p_{\text{astro}} \geq 0.5$ and FAR less than 2 per day, we identified 33 candidate events over O3. This includes 23 in O3a and 10 in O3b. Of these, 31 are consistent with the most up-to-date GWTC catalogs; one candidate (GW190605_025957) was consistent only with the IAS higher-order modes search, IAS-HOM [43], and one was a newly identified candidate that has not been previously reported (GW190929_091722). For candidates identified by our search, we report the p_{astro} , FAR, and network SNR values, as well as the corresponding values from the original offline search that led to their identification, in Table IV. In the case of GWTC being the original search, we include the results from the pipeline (cWB, MBTA, GstLAL, PyCBC or PyCBC-BBH) with the highest p_{astro} , or highest SNR if more than one search pipeline shares the highest p_{astro} . The candidates we jointly detect with existing offline searches are presented in more detail in Section IV A, and we explore the newly detected candi-

date in Section IV B. We investigate the candidates that our search pipeline failed to identify in Section IV C.

A. Existing candidate detections

We see in Table IV that the candidate events identified by our search strongly overlap with the results of the GWTC catalogs, including one of five NSBH candidates, GW190814_211039, that we discuss further in Section IV A 1. In addition, we provide supporting evidence for the identification of one candidate previously identified only by the IAS-HOM search [43] and one new candidate unique to our search. We discuss these two candidates further in Sections IV A 2 and IV B, respectively.

We find two candidate events, GW190731_140936 and GW200216_220804, that are detected with p_{astro} values significantly higher than in their original searches. Both of these candidates were later reported with higher p_{astro} values in the OGC-4 catalog [27], but these updated values are still lower than those assigned by our search. We also find that our p_{astro} for GW200216_220804 is higher despite having a worse FAR than reported in GWTC-

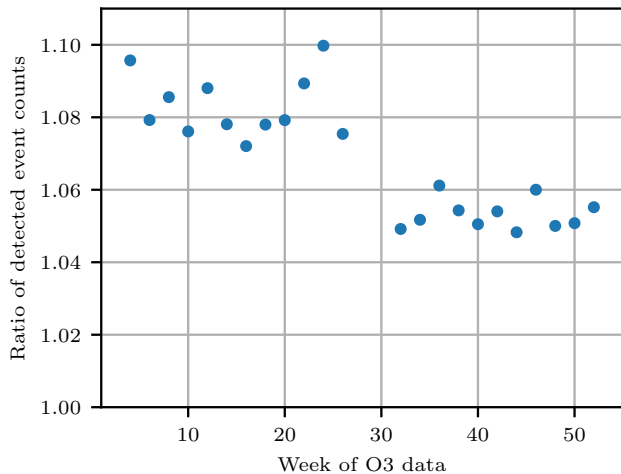


FIG. 8. Ratio of the fraction of detected events from Figure 7 for the combined detection scenario with and without including our search pipeline. Values greater than zero indicate that including our search pipeline increases the number of events detected by at least one search pipeline. The decrease after week 30 suggests that our search pipeline makes fewer unique detections in O3b than in O3a.

3. To understand these behaviors, further investigation is required using injection campaigns to compare p_{astro} values across search pipelines.

1. *GW190814_211039*

Our searched mass space includes a subset of the theoretical neutron star population as our lower mass limit is $2 M_{\odot}$. *GW190814_211039* is one of five potential NSBH candidates in O3 and is the only NSBH candidate we identify in the GWTC catalogs. Our results indicate that we identify it with lower p_{astro} and higher FAR than the search pipelines in the GWTC catalogs, as expected given our observed low sensitivity to low-mass events. It is the lowest chirp mass source to pass our detection threshold, and its significance is likely due to its high network SNR of 22.6.

Improvements to NSBH sensitivity would require training samples that represent a population of NSBH signals rather than just low mass BBH signals, as well as a p_{astro} classifier that considers independent populations of BNS, NSBH and BBH candidates.

2. *GW190605_025957*

This candidate was first reported in the IAS higher-order modes search [43] and is jointly identified for the first time here. This is a reasonably significant result, as offline searches independent of the GWTC catalogues have previously identified 49 additional candidates dur-

ing O3. Of these, only 10 have been jointly identified by independent searches [81], where we do not consider targeted searches (e.g., IAS-HOM) as independent of other searches using the same software framework (IAS-O3a and IAS-O3b). The parameter estimation results for this candidate suggest that it was produced by a high-mass BBH system [43, 81]. However, the candidate has a low SNR, resulting in unconstrained priors.

To test whether this candidate is caused by a glitch or data quality issue, we examine transient noise events and data quality issues, and perform a signal consistency test around the time of the event. To identify excess-power transient events, we use the OMICRON software package [67], which reports one transient in the Livingston detector. This transient has an SNR of 6.05 and a frequency of 41.8 Hz, and occurs within 30 ms of the trigger produced by our search, indicating that this candidate may not be astrophysical. We use the results from the iDQ framework [82, 83] - a machine-learning framework that correlates auxiliary channels with the detector strain - to assess data quality, and we found no significant trigger values near the candidate's event time. Lastly, we employ a reduced χ^2 signal consistency test from the PyCBC search pipeline [84] to determine if the distribution of signal power over frequency bins matches the expectation from the template. We compute the chi-square statistic over a number of bins that depends on the template parameters of the template that produced the trigger in our search pipeline. The formula can be found in the OGC-4 data release⁵ [27]. To compute the PyCBC reweighted SNR statistic, the signal SNR would be down-weighted by a factor of 0.908 in the Hanford detector and 0.987 in the Livingston detector by considering Eqn. 5 in Ref. [84]. These checks suggest that further investigation of the nature of this candidate may be required to determine if it originates from an astrophysical signal.

B. New candidate event

We also report, for the first time, the identification of a candidate event, *GW190929_091722*, at GPS time 1253783860.8. We present the Hanford and Livingston SNR time series and time-frequency spectrograms around the event time in Figure 9. Existing searches do not detect this candidate event, and there are no coincident candidates in the sub-threshold candidate releases as part of the GWTC [85, 86] and OGC [26, 27] catalogs.

In Figure 9, we include a star symbol to highlight the SNR peaks, identified by our peak finding algorithm, associated with the trigger that identifies this candidate. We see that the SNR peak in the Hanford detector is below 4. In contrast, existing multi-detector matched-filter searches consider only trigger times when more than one

⁵ <https://github.com/gwastro/4-ogc>

Name	Catalog	This Work			Original Search		
		p_{astro}	FAR (yr ⁻¹)	SNR	p_{astro}	FAR (yr ⁻¹)	SNR
GW190408_181802	GWTC-2.1	1.00	1.5×10^{-5}	14.0	1.00	$< 1.0 \times 10^{-5}$	14.7
GW190412_053044	GWTC-2.1	1.00	7.8×10^{-6}	17.2	1.00	$< 1.0 \times 10^{-5}$	19.0
GW190413_134308	GWTC-2.1	0.84	2.0	9.7	0.99	0.34	10.3
GW190421_213856	GWTC-2.1	0.99	0.067	10.1	1.00	0.0028	10.5
GW190503_185404	GWTC-2.1	1.00	5.9×10^{-4}	12.5	1.00	0.013	12.8
GW190517_055101	GWTC-2.1	1.00	1.1×10^{-3}	10.2	1.00	0.11	11.3
GW190519_153544	GWTC-2.1	1.00	0.0036	13.8	1.00	7.0×10^{-5}	13.7
GW190521_074359	GWTC-2.1	1.00	2.6×10^{-9}	22.9	1.00	$< 1.0 \times 10^{-5}$	24.4
GW190527_092055	GWTC-2.1	0.82	4.3	8.2	0.85	0.23	8.7
GW190602_175927	GWTC-2.1	1.00	0.0020	12.0	1.00	3.0×10^{-4}	12.6
GW190605_025957	IAS-HOM	0.78	4.6	8.7	0.88	1.7	9.5
GW190706_222641	GWTC-2.1	1.00	1.6×10^{-5}	12.4	1.00	0.34	12.6
GW190707_093326	GWTC-2.1	1.00	0.0090	12.3	1.00	$< 1.0 \times 10^{-5}$	13.2
GW190727_060333	GWTC-2.1	1.00	5.8×10^{-5}	11.6	1.00	$< 1.0 \times 10^{-5}$	12.1
GW190728_064510	GWTC-2.1	1.00	0.0041	12.4	1.00	$< 1.0 \times 10^{-5}$	13.4
GW190731_140936	GWTC-2.1	0.97	0.52	8.4	0.83	1.9	7.8
GW190803_022701	GWTC-2.1	0.99	0.21	8.7	0.97	0.39	8.7
GW190814_211039 [†]	GWTC-2.1	0.68	0.17	22.6	1.00	$< 1.0 \times 10^{-5}$	22.2
GW190828_063405	GWTC-2.1	1.00	3.1×10^{-8}	15.1	1.00	$< 1.0 \times 10^{-5}$	16.3
GW190828_065509	GWTC-2.1	0.88	1.3	10.0	1.00	3.5×10^{-5}	11.1
GW190915_235702	GWTC-2.1	1.00	3.7×10^{-6}	12.4	1.00	$< 7.0 \times 10^{-5}$	13.1
GW190929_012149	GWTC-2.1	0.88	1.8	9.2	0.87	0.16	10.1
GW190929_091722	This Work	0.63	27	6.7
GW191109_010717	GWTC-3	1.00	1.3×10^{-4}	16.1	> 0.99	0.001	15.8
GW191129_134029	GWTC-3	1.00	7.3×10^{-4}	12.5	> 0.99	$< 1.0 \times 10^{-5}$	13.3
GW191215_223052	GWTC-3	0.89	0.56	10.1	> 0.99	$< 1.0 \times 10^{-5}$	10.9
GW191222_033537	GWTC-3	1.00	2.3×10^{-4}	11.8	> 0.99	$< 1.0 \times 10^{-5}$	12.0
GW200129_065458	GWTC-3	1.00	3.2×10^{-8}	24.3	> 0.99	$< 1.0 \times 10^{-5}$	26.5
GW200208_130117	GWTC-3	0.92	0.53	9.5	> 0.99	3.1×10^{-4}	10.8
GW200209_085452	GWTC-3	0.99	0.044	9.4	0.97	12	9.7
GW200216_220804	GWTC-3	0.85	1.5	8.8	0.77	0.35	9.4
GW200224_222234	GWTC-3	1.00	7.0×10^{-8}	17.9	> 0.99	$< 8.2 \times 10^{-5}$	19.2
GW200311_115853	GWTC-3	1.00	1.3×10^{-6}	15.7	> 0.99	$< 1.0 \times 10^{-5}$	17.7

TABLE IV. Search pipeline trigger properties of events identified by our search during the third observing run with a probability of astrophysical origin (p_{astro}) greater than or equal to 0.5 and an FAR less than 2 per day. Original search refers to the first offline search to identify an event with $p_{\text{astro}} \geq 0.5$, as reported in the catalog column; in the case of GWTC, it is the results of the most significant individual search pipeline for that event. GW190814_211039 is indicated with a [†] due to it being a potential NSBH candidate, although it cannot be ruled out as a BBH candidate.

detector peaks above an SNR of 4. Since we do not train our model on low SNR and single detector samples, and we tune our p_{astro} model on a set of injections with a minimum network SNR of 6, there is a reasonable amount of uncertainty in our p_{astro} calculation. Additionally, the Hanford peak identified by our algorithm is not associated with the higher SNR feature that occurs approximately 30 ms post-merger. A common concern in developing deep learning models is explainability, as it is often

unclear which aspects of the input data the model relies on to make its predictions. In this case, the candidate's SNR time series underscores the need to examine how deep learning models behave in practice when detecting coincident signals. In particular, we must ensure that the model relies only on astrophysically relevant features.

As we did for GW190605_025957, we conducted a series of data quality checks to validate the data around the candidate event. A search for transient noise events

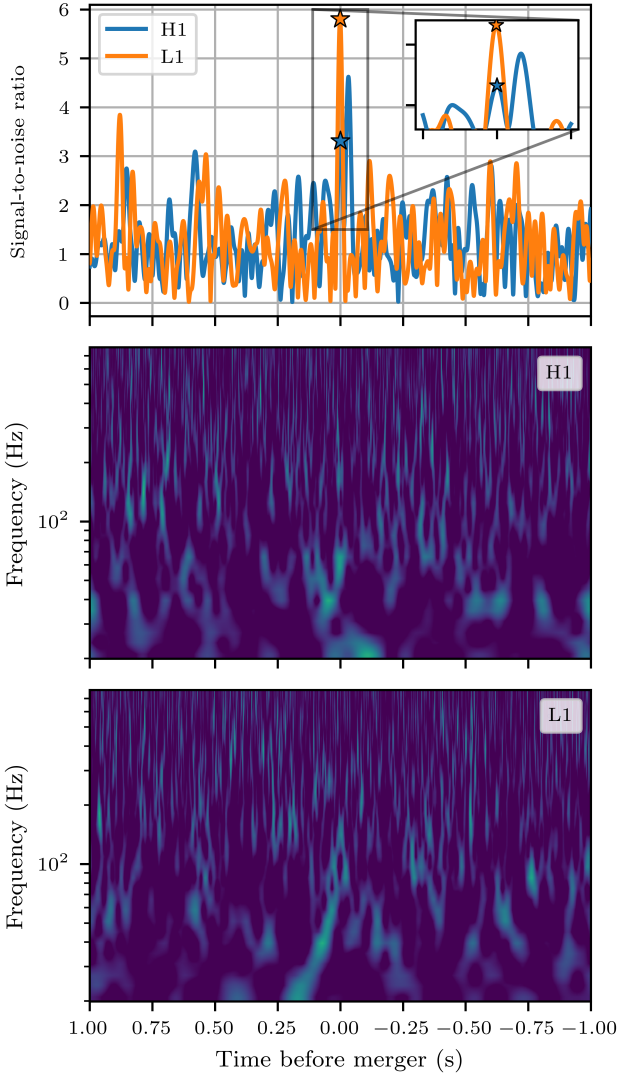


FIG. 9. SNR time series and time-frequency spectrograms of the strain data for our new candidate event GW190929_091722. The stars on the SNR time series represent the values from the trigger that identified the event, highlighting a larger SNR peak in the Hanford detector (H1) outside the light-travel time from the peak in the Livingston detector (L1).

with OMICRON returned no triggers with an SNR greater than 5 at a frequency that would appear in the SNR time series. Two transients were identified by OMICRON in the Hanford detector at ~ 446 Hz and ~ 1345 Hz with SNRs of 5.03 and 5.56, respectively, and were labeled as occurring at least 30 ms after the candidate’s merger time. Since these transients occur at high frequencies, have low SNRs, and appear after the candidate merger time, we do not expect them to interfere with identifying this candidate, which was done using a high-mass, short-duration template. We also find that no significant trigger values were produced by the iDQ framework around this

event [83]. Lastly, the reduced χ^2 was < 1 in both the Hanford and Livingston detectors, which would result in no scaling of the SNR to get the PyCBC re-weighted SNR statistic [84]. These findings suggest that there are no data-quality or transient-noise issues with the data surrounding this candidate event.

1. Parameter estimation

For our new candidate event, we based our parameter estimation analysis on Ref. [81] and used the ASIMOV software framework [87, 88] to manage and complete the parameter estimation workflows. We used BAYESWAVE [89, 90] to produce on-source PSD estimates in both the Hanford and Livingston detectors. These PSDs were used with BILBY [91] for model selection with the dynesty nested sampler [92], together with the IMR-PhenomXPHM waveform model [93]. We also used the PESUMMARY package [94] for plotting and analysis of the posterior estimates produced by BILBY. We provide the necessary ASIMOV configuration files, as well as the resulting posterior samples, as part of an associated data release on GitHub⁶.

We present the results of this analysis for a subset of the source parameters in Table V and Figure 10. We see that this candidate is consistent with a high mass BBH binary with a total mass, M , of $171_{-58}^{+172} M_{\odot}$, which is a larger median than any GWTC-3 [8] candidate and the third highest median compared with the other searches in the Beyond GWTC-3 parameter estimation catalog [81].

Existing black hole formation models present the case that black holes cannot be expected to be formed through stellar collapse if the black hole mass is in the range of $65 < m < 120$ [95–104], and that some other formation channel is required. In this mass range, we expect a progenitor to encounter pair-instability supernovae, leaving no remnant behind. Our posterior results for GW190929_091722 suggest that the primary component has a 51.6% probability of having a mass within this range, and the secondary component has a 34.7% probability. Additionally, our primary component has a 44.5% probability of having a mass greater than $120 M_{\odot}$.

Our parameter estimation results indicate that, if astrophysical, this candidate could lie outside the mass parameter space on which our deep learning model is trained, thereby affecting the significance with which we recover it. To account for this, an intermediate-mass black hole search should be conducted to verify our search results for this candidate event. The LVK Collaboration performed an offline IMBH search in O3 [105], and found no candidates coincident with our new candidate. We see no other notable results from this parameter estimation

⁶ https://github.com/damonbeveridge/new_BBH_O3_candidate-UWA

M (M_\odot)	\mathcal{M} (M_\odot)	m_1 (M_\odot)	m_2 (M_\odot)	χ_{eff}	D_L (Gpc)	z	M_f (M_\odot)	χ_f	$\Delta\Omega(\text{deg}^2)$	SNR
171^{+172}_{-58}	68.0^{+53}_{-25}	114^{+162}_{-47}	57.5^{+48}_{-33}	$0.21^{+0.45}_{-0.47}$	$7.02^{+8.25}_{-4.20}$	$1.03^{+0.90}_{-0.54}$	164^{+169}_{-55}	$0.76^{+0.16}_{-0.25}$	15000	$5.55^{+0.78}_{-1.37}$

TABLE V. Median and 90% symmetric credible intervals for select source parameters of our new candidate event, GW190929_091722. The columns show the total mass of the binary, M ; the chirp mass, \mathcal{M} ; the component masses, m_1 and m_2 ; the effective dimensionless spin parameter, χ_{eff} ; the luminosity distance, D_L ; the redshift, z ; the final mass, M_f ; the dimensionless final spin χ_f ; the sky localization area, $\Delta\Omega$; and the network matched-filter SNR. All quoted results for masses are in the source frame.

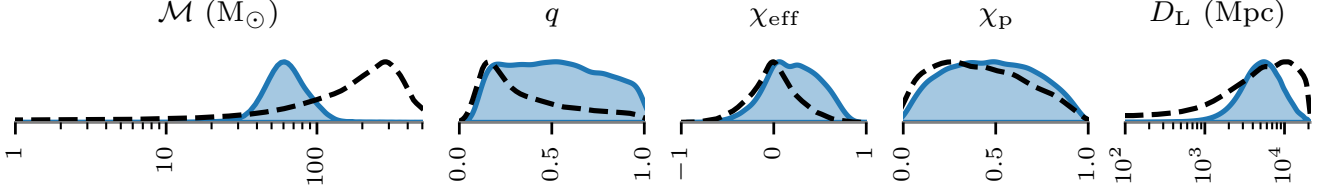


FIG. 10. Parameter estimation results for our new candidate event, GW190929_091722. From left to right are the source frame chirp mass, \mathcal{M} ; the mass ratio, q ; the effective dimensionless spin parameter, χ_{eff} ; the precessing dimensionless spin parameter, χ_p ; and the luminosity distance, D_L . The blue region represents the posterior probability distributions from our analysis, and the black dotted line represents the prior distributions.

analysis, mainly due to the low SNR and short duration of the candidate.

C. Missed candidates

Equally important as the candidates we detect are those we fail to recover. Examining missed events highlights the current limitations of our pipeline. We display the candidate events that our search fails to identify throughout O3a and O3b in Table VI and Table VII, respectively. We include the results of our search pipeline in these tables when a trigger is produced with an FAR of less than 2 per day.

In Section IV C 1 below, we discuss the candidate events that are not included in Tables VI and VII due to design choices of our search pipeline that prevent us from being able to detect these events. Section IV C 2 discusses the remaining candidate events that are considered detectable by our search pipeline, and we give reasoning for why these candidates are not detected.

1. Hopeless candidates

Excluded from Tables VI and VII are 11 events due to no coincident Hanford and Livingston detector data, including six in O3a and three in O3b from the GWTC-3 catalog, as well as one in each of the observation runs from the OGC catalog. Additionally, we miss GW190911_195101 because it occurs in a data segment with a duration less than 1024 seconds, which we exclude from our search as per Section II A.

Since our search pipeline clusters SNR triggers across the entire template bank using our peak-finding algorithm, we find that it has missed four events due to glitch interference. We miss these events when long-duration templates produce high SNR responses to glitches over long timescales that dominate our peak-finding algorithm, even after the glitch has ceased to be present in the strain. The candidates affected by this include GW190514_065416, GW190818_232544, GW191204_171526, and GW191219_163120, the latter of which has source properties consistent with an NSBH event. An example of this behavior is shown in Figure 11, which displays the SNR time series of the highest-SNR template identified by our peak-finding algorithm for GW191204_171526. The PyCBC search pipeline overcomes this by performing peak-finding and producing a ranking statistic across 15 separate clusters of their template bank, then marginalizing over these clusters by selecting the trigger with the most significant ranking statistic [24]. This feature can be integrated into our search pipeline in the future, particularly as we expand it to identify BNS, NSBH, and BBH candidates. From a preliminary analysis comparing the recovered SNR to the injected SNR of our injection campaign during the O3 observing run, this feature may make over a thousand injections now detectable by our search, which could provide a meaningful increase in our sensitivity results.

Since our search involves a matched-filter analysis, we lose the ability to identify events in the first 200 seconds and the last 24 seconds of a data segment, as outlined in Section II A. The 200-second cuts account for four missed events from the GWTC catalogs - GW190701_203306, GW190725_174728,

Name	Catalog	$\mathcal{M} (M_{\odot})$	q	This Work			Original Search		
				p_{astro}	FAR (yr^{-1})	SNR	p_{astro}	FAR (yr^{-1})	SNR
GW190403_051519	GWTC-2.1	$34.0^{+15.1}_{-8.4}$	$0.23^{+0.57}_{-0.12}$	0.61	7.7	8.0
GW190404_142514	OGC-4	$13.8^{+2.2}_{-1.9}$	$0.56^{+0.36}_{-0.27}$	0.50	50	7.8
GW190413_052954	GWTC-2.1	$24.6^{+5.5}_{-4.1}$	$0.73^{+0.24}_{-0.31}$	0.27	44	8.7	0.93	0.82	8.5
GW190426_082124	AresGW	$28.9^{+8.7}_{-7.4}$	$0.70^{+0.26}_{-0.34}$	0.50	20	-
GW190426_190642	GWTC-2.1	$76.0^{+19.1}_{-17.4}$	$0.76^{+0.22}_{-0.48}$	0.75	4.1	9.6
GW190427_180650	OGC-4	$7.3^{+0.6}_{-0.6}$	$0.54^{+0.38}_{-0.26}$	0.53	50	8.9
GW190511_125545	AresGW	$27.2^{+9.7}_{-7.6}$	$0.61^{+0.34}_{-0.33}$	1.00	0.27	-
GW190511_163209	IAS-HOM	$39.2^{+35.5}_{-23.6}$	$0.27^{+0.59}_{-0.16}$	0.61	12	9.5
GW190512_180714	GWTC-2.1	$14.6^{+1.3}_{-1.0}$	$0.54^{+0.36}_{-0.18}$	0.24	18	11.2	1.00	$<1.1 \times 10^{-4}$	12.4
GW190521_030229	GWTC-2.1	$69.2^{+17.0}_{-10.6}$	$0.59^{+0.33}_{-0.38}$	0.06	36	14.4	1.00	0.0013	13.6
GW190523_085933	AresGW	$23.2^{+18.0}_{-12.0}$	$0.38^{+0.53}_{-0.21}$	0.68	20	-
GW190524_134109	IAS-HOM	$46.0^{+16.8}_{-13.8}$	$0.66^{+0.30}_{-0.44}$	0.05	444	8.0	0.85	2.3	8.2
GW190530_030659	IAS-HOM	$21.4^{+3.7}_{-3.7}$	$0.61^{+0.33}_{-0.35}$	0.04	578	7.8	0.63	11	8.4
GW190530_133833	IAS-HOM	$58.6^{+23.6}_{-20.6}$	$0.59^{+0.37}_{-0.39}$	0.53	17	8.4
GW190604_103812	IAS-HOM	$55.4^{+31.5}_{-25.5}$	$0.35^{+0.48}_{-0.21}$	0.68	7.7	8.2
GW190607_083827	AresGW	$31.6^{+7.4}_{-6.6}$	$0.77^{+0.21}_{-0.31}$	0.99	6.5	-
GW190614_134749	AresGW	$26.3^{+9.6}_{-7.6}$	$0.60^{+0.35}_{-0.33}$	0.99	4.6	-
GW190615_030234	IAS-HOM	$49.8^{+12.5}_{-10.9}$	$0.75^{+0.22}_{-0.37}$	0.75	5.0	8.6
GW190704_104834 [‡]	IAS-O3a	$4.2^{+0.1}_{-0.1}$	$0.52^{+0.38}_{-0.29}$	0.81	0.36	8.9
GW190705_164632	AresGW	$33.6^{+11.2}_{-10.3}$	$0.57^{+0.38}_{-0.32}$	0.51	49	-
GW190707_083226	IAS-O3a	$35.9^{+8.9}_{-7.9}$	$0.63^{+0.32}_{-0.34}$	0.94	0.043	8.3
GW190711_030756	IAS-O3a	$31.1^{+6.7}_{-6.4}$	$0.34^{+0.36}_{-0.21}$	0.93	0.089	9.0
GW190718_160159	IAS-O3a	$7.0^{+0.7}_{-0.7}$	$0.68^{+0.28}_{-0.41}$	0.53	2.1	8.4
GW190719_215514	GWTC-2.1	$23.5^{+6.5}_{-4.0}$	$0.55^{+0.40}_{-0.41}$	0.10	177	8.3	0.92	0.63	8.0
GW190720_000836	GWTC-2.1	$8.9^{+0.5}_{-0.8}$	$0.53^{+0.36}_{-0.24}$	0.12	65	10.1	1.00	0.094	11.6
GW190805_105432	OGC-4	$8.8^{+0.8}_{-0.8}$	$0.52^{+0.37}_{-0.20}$	0.51	50	8.1
GW190805_211137	GWTC-2.1	$31.9^{+8.8}_{-6.3}$	$0.68^{+0.28}_{-0.33}$	0.95	0.63	8.3
GW190806_033721	IAS-HOM	$42.4^{+15.2}_{-12.8}$	$0.49^{+0.44}_{-0.30}$	0.86	2.2	8.3
GW190814_192009	IAS-O3a	$50.3^{+17.2}_{-13.9}$	$0.71^{+0.26}_{-0.40}$	0.64	1.5	8.0
GW190821_124821 [‡]	IAS-O3a	$4.8^{+0.3}_{-0.2}$	$0.28^{+0.28}_{-0.11}$	0.60	1.4	8.8
GW190904_104631	AresGW	$26.1^{+15.8}_{-15.3}$	$0.61^{+0.34}_{-0.34}$	0.72	14	-
GW190906_054335	IAS-O3a	$25.7^{+8.4}_{-8.0}$	$0.63^{+0.33}_{-0.36}$	0.61	1.4	7.9
GW190910_012619	IAS-O3a	$9.6^{+0.8}_{-0.9}$	$0.12^{+0.04}_{-0.02}$	0.58	1.5	8.2
GW190916_200658	GWTC-2.1	$26.9^{+8.2}_{-5.4}$	$0.55^{+0.40}_{-0.32}$	0.44	30	7.9	0.66	6900	8.2
GW190917_114630 [†]	GWTC-2.1	$3.7^{+0.2}_{-0.2}$	$0.21^{+0.32}_{-0.09}$	0.77	0.66	9.5
GW190920_113516 [‡]	IAS-O3a	$3.8^{+0.2}_{-0.2}$	$0.52^{+0.38}_{-0.29}$	0.57	1.8	8.6
GW190924_021846	GWTC-2.1	$5.8^{+0.2}_{-0.2}$	$0.58^{+0.32}_{-0.30}$	0.07	61	11.9	1.00	$<1.0 \times 10^{-5}$	13.0
GW190926_050336	GWTC-2.1	$24.4^{+9.0}_{-4.9}$	$0.50^{+0.42}_{-0.26}$	0.54	1.1	9.0
GW190930_133541	GWTC-2.1	$8.5^{+0.5}_{-0.5}$	$0.49^{+0.43}_{-0.27}$	0.45	11	10.1	1.00	0.012	10.0

TABLE VI. Properties of missed events during the O3a observing run that are detectable according to Section IV C 1. Original search refers to the first offline search that identifies an event. For GWTC-3 candidates, the results are from the most significant (highest p_{astro}) search pipeline for that event. The dagger ([†]) indicates a candidate with masses consistent with an NSBH system, and a double dagger ([‡]) indicates a candidate that is possibly consistent with originating from an NSBH or BBH source. Ellipses (...) indicate that our search pipeline does not produce a trigger with an FAR < 2 per day.

Name	Catalog	$\mathcal{M} (M_{\odot})$	q	This Work			Original Search		
				p_{astro}	FAR (yr^{-1})	SNR	p_{astro}	FAR (yr^{-1})	SNR
GW191103_012549	GWTC-3	$8.3^{+0.7}_{-0.6}$	$0.67^{+0.29}_{-0.37}$	0.94	0.46	9.3
GW191105_143521	GWTC-3	$7.8^{+0.6}_{-0.5}$	$0.72^{+0.24}_{-0.31}$	>0.99	0.14	10.7
GW191113_071753	GWTC-3	$10.7^{+1.1}_{-1.0}$	$0.20^{+0.49}_{-0.09}$	0.68	26	9.2
GW191113_103541	IAS-HOM	$36.3^{+13.3}_{-9.7}$	$0.20^{+0.18}_{-0.07}$	0.76	4.8	8.7
GW191117_023843	IAS-O3b	$38.3^{+9.7}_{-7.9}$	$0.26^{+0.17}_{-0.14}$	0.56	8.3	8.0
GW191126_115259	GWTC-3	$8.7^{+1.0}_{-0.7}$	$0.69^{+0.28}_{-0.35}$	0.70	3.2	8.5
GW191127_050227	GWTC-3	$29.9^{+11.7}_{-9.1}$	$0.47^{+0.47}_{-0.35}$	0.74	4.1	8.7
GW191204_110529	GWTC-3	$19.8^{+3.6}_{-3.2}$	$0.73^{+0.24}_{-0.35}$	0.74	3.3	8.9
GW191224_043228	OGC-4	$9.3^{+0.9}_{-0.8}$	$0.51^{+0.39}_{-0.22}$	0.87	7.7	8.4
GW191228_085854	IAS-O3b	$6.3^{+0.2}_{-0.2}$	$0.57^{+0.20}_{-0.27}$	0.67	4.0	9.0
GW191228_195619	IAS-HOM	$96.0^{+40.4}_{-31.8}$	$0.46^{+0.32}_{-0.22}$	0.67	8.3	10.5
GW191230_180458	GWTC-3	$36.5^{+8.2}_{-5.6}$	$0.77^{+0.20}_{-0.34}$	0.48	5.4	10.0	0.96	0.42	9.9
GW200106_134123	OGC-4	$29.7^{+7.4}_{-7.2}$	$0.63^{+0.32}_{-0.30}$	0.45	20	7.5	0.69	17	7.4
GW200109_195634	IAS-O3b	$44.9^{+12.7}_{-11.7}$	$0.72^{+0.25}_{-0.37}$	0.32	26	8.0	0.81	1.1	8.0
GW200115_042309 [†]	GWTC-3	$2.4^{+0.1}_{-0.1}$	$0.24^{+0.43}_{-0.10}$	0.02	227	10.4	>0.99	$<1.0 \times 10^{-5}$	11.5
GW200128_022011	GWTC-3	$32.0^{+7.5}_{-5.5}$	$0.80^{+0.18}_{-0.30}$	>0.99	0.0043	9.9
GW200129_114245	OGC-4	$43.1^{+16.0}_{-15.6}$	$0.45^{+0.44}_{-0.24}$	0.53	25	7.9
GW200202_154313	GWTC-3	$7.5^{+0.2}_{-0.2}$	$0.72^{+0.24}_{-0.31}$	>0.99	$<1.0 \times 10^{-5}$	11.3
GW200208_211609	AresGW	$21.0^{+35.6}_{-14.5}$	$0.72^{+0.24}_{-0.31}$	0.55	18	-
GW200208_222617	GWTC-3	$19.8^{+10.5}_{-5.2}$	$0.21^{+0.67}_{-0.16}$	0.70	4.8	7.9
GW200210_005122	OGC-4	$6.4^{+0.5}_{-0.4}$	$0.67^{+0.29}_{-0.33}$	0.74	25	8.3
GW200210_092254 [‡]	GWTC-3	$6.6^{+0.4}_{-0.4}$	$0.12^{+0.05}_{-0.04}$	0.54	7.7	8.9
GW200210_100022	IAS-O3b	$29.1^{+8.9}_{-7.3}$	$0.17^{+0.20}_{-0.06}$	0.52	10	7.8
GW200219_094415	GWTC-3	$27.6^{+5.6}_{-3.8}$	$0.77^{+0.21}_{-0.32}$	0.07	67	10.1	>0.99	9.9×10^{-4}	10.7
GW200220_061928	GWTC-3	$62.2^{+22.8}_{-15.1}$	$0.73^{+0.24}_{-0.41}$	0.62	6.8	7.5
GW200220_124850	GWTC-3	$28.2^{+7.3}_{-5.1}$	$0.74^{+0.23}_{-0.33}$	0.83	1800	8.2
GW200225_060421	GWTC-3	$14.2^{+1.5}_{-1.4}$	$0.73^{+0.23}_{-0.28}$	>0.99	$<8.8 \times 10^{-4}$	13.1
GW200225_075134	IAS-O3b	$42.8^{+9.0}_{-7.9}$	$0.77^{+0.20}_{-0.31}$	0.60	6.7	8.3
GW200301_211019	IAS-HOM	$14.5^{+2.1}_{-2.1}$	$0.63^{+0.31}_{-0.40}$	0.56	14	8.6
GW200304_172806	IAS-HOM	$52.6^{+21.9}_{-19.6}$	$0.49^{+0.45}_{-0.35}$	0.66	9.1	8.3
GW200305_084739	OGC-4	$24.0^{+5.6}_{-4.7}$	$0.75^{+0.22}_{-0.35}$	0.59	50	7.6
GW200306_093714	GWTC-3	$17.5^{+3.5}_{-3.0}$	$0.53^{+0.40}_{-0.33}$	0.81	410	8.5
GW200308_173609	GWTC-3	$34.2^{+43.8}_{-17.5}$	$0.39^{+0.48}_{-0.29}$	0.86	2.4	8.0
GW200316_235947 [‡]	IAS-O3b	$4.2^{+0.2}_{-0.2}$	$0.57^{+0.33}_{-0.37}$	0.52	11	8.3
GW200318_191337	OGC-4	$31.9^{+8.5}_{-6.5}$	$0.70^{+0.26}_{-0.34}$	0.97	2	7.8
GW200322_091133	GWTC-3	$15.0^{+29.5}_{-4.0}$	$0.29^{+0.63}_{-0.26}$	0.62	450	9.0

TABLE VII. Properties of missed events during the O3b observing run that are detectable according to Section IV C 1. Original search refers to the first offline search that identifies an event. For GWTC-3 candidates, the results are from the most significant (highest p_{astro}) search pipeline for that event. The dagger ([†]) indicates a candidate with masses consistent with an NSBH system, and a double dagger ([‡]) indicates a candidate that is possibly consistent with originating from an NSBH or BBH source. Ellipses (...) indicate that our search pipeline does not produce a trigger with an FAR < 2 per day.

GW200214.223307, GW200316.215756 - and the 24-second cuts account for one event - GW190513.205428. Suppose we were to develop our search pipeline further to identify short-duration templates within the first 200 seconds of a data segment. It may then be possible to detect the four missed events, as they should be

short enough signals within the detector sensitivity bands based on their inferred masses [8]. The 24-second window at the end of a data segment was chosen as a conservative value, and should be able to be reduced in the future. Reducing this window could help our search identify GW190513.205428, which exists approximately

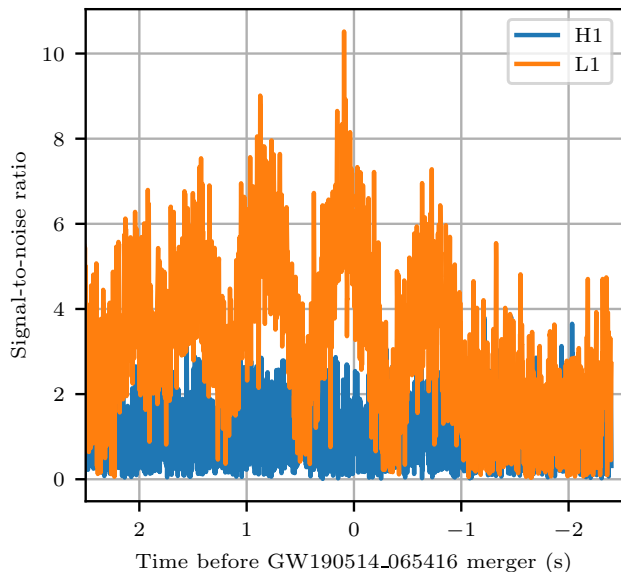


FIG. 11. SNR time series for the template that produced the trigger in our search pipeline nearest to the event GW190514_065416. This template has a detector frame chirp mass of $2.9 M_{\odot}$. In contrast, GW190514_065416 has an estimated detector-frame chirp mass of $48.6 M_{\odot}$, demonstrating that our search pipeline is susceptible to long-duration templates broadening the temporal response of a short-duration glitch, resulting in missed detections.

21 seconds before the end of a data segment.

2. Detectable candidates

In this section, we relate trends from our injection sensitivity tests to the population of remaining missed events in our O3 search. We discuss only the events listed in Tables VI and VII for which our search pipeline has the opportunity to detect candidates. This includes 39 events in O3a and 36 events in O3b.

The most notable lack of sensitivity we observed in our injection studies (Section III) is at lower masses. More specifically, we observe a drop-off in sensitivity relative to the other matched-filter searches below a source-frame chirp mass of $25 M_{\odot}$ and a network SNR of 15. By considering the median source frame chirp masses from parameter estimation [6, 7, 27, 41, 42, 81] and the original search SNRs of the events in Tables VI and VII, this accounts for 18 of 39 events in O3a and 19 of 36 in O3b, including four (three) potential NSBH candidates in O3a (O3b). Extending this selection to events where the parameter estimation results indicate that the 90% credible region for the source-frame chirp mass is less than $25 M_{\odot}$ results in 28 of 39 missed events in O3a and 26 of 36 in O3b.

Of the remaining 21 missed candidates throughout O3, nine candidates have a mass ratio, q , less than 0.5. In

Section III, we observed the possibility that our search has a reduced sensitivity for higher mass events with a low mass ratio. However, these sensitivity results are not conclusive, so we cannot conclusively attribute this to the failure to detect these events. Of these low mass ratio events, GW190604_103812, GW191113_103541 and GW191228_195619 have a median primary component mass greater than $100 M_{\odot}$, which is outside our trained parameter space. The remaining three events with $q < 0.5$ in each O3a and O3b have primary component masses with 90% credible intervals extending above $100 M_{\odot}$ as well.

There remain eight (six) missed events in O3a (O3b) for which we have not provided reasoning through a link to our injection sensitivity results. We find that in O3a, GW190426_190642 has a median primary-component mass above our training parameter space. Additionally, GW190530_133833 and GW200220_061928 have posterior support within the 90% credible interval for a primary component mass exceeding the limits of our training parameter space.

Of the remaining 11 events throughout O3 that we do not detect, our search pipeline does produce triggers with an FAR of less than 2 per day for three candidates. Our search identified GW191230_180458 with a p_{astro} of 0.48, and GW200109_195634 with a p_{astro} of 0.32, so we do not consider missing these events problematic. We produced a trigger for GW190524_134109 with a p_{astro} of 0.05; however, this event has been identified only by the IAS-HOM [43].

Three of the remaining eight candidates that we do not produce triggers for are supported by detections from more than one independent search pipeline: GW190607_083827 [47, 53], GW200128_022011 [8], and GW200318_191337 [27, 47]. Since the remaining five candidates cannot be explicitly treated as astrophysical due to low SNR and a lack of supporting detections across independent searches, we are not concerned about not detecting them.

While we have demonstrated a link between our injection sensitivity results and the population of missed events, it does not necessarily explain why there are so many missed events. It is essential to note that, although one or more searches have identified a candidate, it does not necessarily mean that the candidate event is guaranteed to originate from an astrophysical source. If we only consider candidate events from the LVK's GWTC-3 catalog [8], we have identified 31 of 79 candidates throughout O3, with only 63 of those being detectable based on constraints outlined in Section IVC 1. Additionally, our injection studies revealed a large number of unique detections, resulting in less overlap between the detected populations of our search pipeline and the others, which may be translated into our search for real events.

V. CONCLUSION

In this work, we conducted an injection sensitivity study and an offline search for BBH gravitational waves during O3. Unlike traditional pipelines that rely on analytical metrics to identify signals, we built a hybrid search pipeline that uses a deep learning classifier to predict from the SNR time series produced by matched filtering. The current version of the search pipeline demonstrates comparable sensitivity to existing searches for high-stellar-mass black holes, yielding a large number of unique detections that significantly enhance the combined search sensitivity of existing pipelines. Our observed low sensitivity at low masses is not a concern for future applications of this search method, given past research demonstrating its capabilities at low masses; therefore, a revised training and optimization approach is required. We demonstrate that this search method can detect 31 previously identified gravitational wave candidate events from the GWTC catalogues, as well as one candidate from the IAS higher-order modes search and a new candidate that has not been previously reported. Several more candidates have been identified with high significance by the GWTC, OGC, IAS and AresGW offline searches, and we have provided a link between our injection sensitivity results and the population of missed candidates.

We have discussed several areas for improvement in our search pipeline as we progress to developing a search that can identify BNS, NSBH and BBH candidates together. These include optimizing training datasets and training metrics to ensure consistent sensitivity levels across the parameter space, improving sensitivity over long observing runs so that models do not need to be retrained regularly, and updating our p_{astro} model to model our ranking

statistic and source populations more accurately and to classify between source types.

There are also more specific pipeline improvements that could be adapted from existing search pipelines, such as clustering regions of the template bank to identify BBH events in the presence of loud glitches, which resulted in four missed candidates. Additional potential changes include adjusting our SNR time-series peak-finding algorithm to account for calibration uncertainties in the light travel time between detectors and to require coincident triggers between detectors. Lastly, extending our search to single-detector and other two-detector configurations will increase our capacity to identify events beyond times when the Hanford and Livingston detectors are operating in coincidence. Furthermore, adding a three-detector search with the Virgo detector could increase confidence in detections.

ACKNOWLEDGMENTS

We thank Siddharth Soni for their assistance in providing Omicron glitch identification results for the O3 observing run. This work was performed on the OzSTAR national facility at Swinburne University of Technology. The OzSTAR program receives funding in part from the Astronomy National Collaborative Research Infrastructure Strategy (NCRIS) allocation provided by the Australian Government, and from the Victorian Higher Education State Investment Fund (VHESIF) provided by the Victorian Government. This material is based upon work supported by NSF's LIGO Laboratory which is a major facility fully funded by the National Science Foundation. The authors are grateful for computational resources provided by the LIGO Laboratory and supported by National Science Foundation Grants PHY-0757058 and PHY-0823459.

-
- [1] B. P. Abbott *et al.* (LIGO-Virgo-KAGRA Collaboration), Prospects for observing and localizing gravitational-wave transients with Advanced LIGO, Advanced Virgo and KAGRA, [Living Reviews in Relativity](#) **23**, 3 (2020).
 - [2] J. Aasi *et al.* (LIGO Scientific), Advanced LIGO, [Class. Quant. Grav.](#) **32**, 074001 (2015), [arXiv:1411.4547 \[gr-qc\]](#).
 - [3] F. Acernese *et al.* (VIRGO), Advanced Virgo: a second-generation interferometric gravitational wave detector, [Class. Quant. Grav.](#) **32**, 024001 (2015), [arXiv:1408.3978 \[gr-qc\]](#).
 - [4] T. Akutsu *et al.* (KAGRA), Overview of KAGRA: Detector design and construction history, [PTEP](#) **2021**, 05A101 (2021), [arXiv:2005.05574 \[physics.ins-det\]](#).
 - [5] B. P. Abbott *et al.* (LIGO Scientific, Virgo), GWTC-1: A Gravitational-Wave Transient Catalog of Compact Binary Mergers Observed by LIGO and Virgo during the First and Second Observing Runs, [Phys. Rev. X](#) **9**, 031040 (2019), [arXiv:1811.12907 \[astro-ph.HE\]](#).
 - [6] R. Abbott *et al.* (LIGO Scientific, Virgo), GWTC-2: Compact Binary Coalescences Observed by LIGO and Virgo During the First Half of the Third Observing Run, [Phys. Rev. X](#) **11**, 021053 (2021), [arXiv:2010.14527 \[gr-qc\]](#).
 - [7] R. Abbott *et al.* (LIGO Scientific, VIRGO), GWTC-2.1: Deep extended catalog of compact binary coalescences observed by LIGO and Virgo during the first half of the third observing run, [Phys. Rev. D](#) **109**, 022001 (2024), [arXiv:2108.01045 \[gr-qc\]](#).
 - [8] R. Abbott *et al.* (LIGO Scientific Collaboration, Virgo Collaboration, and KAGRA Collaboration), GWTC-3: Compact Binary Coalescences Observed by LIGO and Virgo during the Second Part of the Third Observing Run, [Phys. Rev. X](#) **13**, 041039 (2023).
 - [9] A. G. Abac *et al.* (LIGO Scientific, VIRGO, KAGRA), GWTC-4.0: Updating the Gravitational-Wave Transient Catalog with Observations from the First

- Part of the Fourth LIGO-Virgo-KAGRA Observing Run (2025), [arXiv:2508.18082 \[gr-qc\]](#).
- [10] B. P. Abbott *et al.* (LIGO Scientific Collaboration and Virgo Collaboration), GW170817: Observation of Gravitational Waves from a Binary Neutron Star Inspiral, *Phys. Rev. Lett.* **119**, 161101 (2017).
 - [11] B. P. Abbott *et al.* (LIGO Scientific, Virgo), GW190425: Observation of a Compact Binary Coalescence with Total Mass $\sim 3.4M_{\odot}$, *Astrophys. J. Lett.* **892**, L3 (2020), [arXiv:2001.01761 \[astro-ph.HE\]](#).
 - [12] R. Abbott *et al.*, Observation of Gravitational Waves from Two Neutron Star-Black Hole Coalescences, *Astrophys. J. Lett.* **915**, L5 (2021), [arXiv:2106.15163 \[astro-ph.HE\]](#).
 - [13] A. G. Abac *et al.* (LIGO-Virgo-KAGRA Collaboration), Observation of Gravitational Waves from the Coalescence of a $2.5\text{--}4.5 M_{\odot}$ Compact Object and a Neutron Star, *Astrophys. J. Lett.* **970**, L34 (2024), [arXiv:2404.04248 \[astro-ph.HE\]](#).
 - [14] R. Abbott *et al.* (LIGO Scientific, Virgo), GW190814: Gravitational Waves from the Coalescence of a 23 Solar Mass Black Hole with a 2.6 Solar Mass Compact Object, *Astrophys. J. Lett.* **896**, L44 (2020), [arXiv:2006.12611 \[astro-ph.HE\]](#).
 - [15] L. S. Collaboration and V. Collaboration, *LIGO/Virgo Public Alerts User Guide*, Tech. Rep. DCC-P1900171 (LIGO, 2019).
 - [16] B. P. Abbott *et al.*, Multi-messenger Observations of a Binary Neutron Star Merger, *Astrophys. J. Lett.* **848**, L12 (2017), [arXiv:1710.05833 \[astro-ph.HE\]](#).
 - [17] R. Abbott *et al.* (LIGO Scientific, Virgo), GW190521: A Binary Black Hole Merger with a Total Mass of $150M_{\odot}$, *Phys. Rev. Lett.* **125**, 101102 (2020), [arXiv:2009.01075 \[gr-qc\]](#).
 - [18] A. G. Abac *et al.* (KAGRA, Virgo, LIGO Scientific), GW250114: Testing Hawking’s Area Law and the Kerr Nature of Black Holes, *Phys. Rev. Lett.* **135**, 111403 (2025), [arXiv:2509.08054 \[gr-qc\]](#).
 - [19] R. Abbott *et al.*, Properties and Astrophysical Implications of the $150 M_{\odot}$ Binary Black Hole Merger GW190521, *Astrophys. J. Lett.* **900**, L13 (2020), [arXiv:2009.01190 \[astro-ph.HE\]](#).
 - [20] B. Edelman, Z. Doctor, and B. Farr, Poking Holes: Looking for Gaps in LIGO/Virgo’s Black Hole Population, *Astrophys. J. Lett.* **913**, L23 (2021), [arXiv:2104.07783 \[astro-ph.HE\]](#).
 - [21] D. Gerosa and M. Fishbach, Hierarchical mergers of stellar-mass black holes and their gravitational-wave signatures, *Nature Astronomy* **5**, 749 (2021), [arXiv:2105.03439 \[astro-ph.HE\]](#).
 - [22] M. Zevin, S. S. Bavera, C. P. L. Berry, V. Kalogera, T. Fragos, P. Marchant, C. L. Rodriguez, F. Antonini, D. E. Holz, and C. Pankow, One Channel to Rule Them All? Constraining the Origins of Binary Black Holes Using Multiple Formation Pathways, *Astrophys. J.* **910**, 152 (2021), [arXiv:2011.10057 \[astro-ph.HE\]](#).
 - [23] R. Abbott *et al.*, Tests of general relativity with binary black holes from the second LIGO-Virgo gravitational-wave transient catalog, *Phys. Rev. D* **103**, 122002 (2021), [arXiv:2010.14529 \[gr-qc\]](#).
 - [24] A. H. Nitz, C. Capano, A. B. Nielsen, S. Reyes, R. White, D. A. Brown, and B. Krishnan, 1-OGC: The first open gravitational-wave catalog of binary mergers from analysis of public Advanced LIGO data, *Astrophys. J.* **872**, 195 (2019), [arXiv:1811.01921 \[gr-qc\]](#).
 - [25] A. H. Nitz, T. Dent, G. S. Davies, S. Kumar, C. D. Capano, I. Harry, S. Mozzon, L. Nuttall, A. Lundgren, and M. Tápai, 2-OGC: Open Gravitational-wave Catalog of binary mergers from analysis of public Advanced LIGO and Virgo data, *Astrophys. J.* **891**, 123 (2020), [arXiv:1910.05331 \[astro-ph.HE\]](#).
 - [26] A. H. Nitz, C. D. Capano, S. Kumar, Y.-F. Wang, S. Kastha, M. Schäfer, R. Dhurkunde, and M. Cabero, 3-OGC: Catalog of Gravitational Waves from Compact-binary Mergers, *Astrophys. J.* **922**, 76 (2021), [arXiv:2105.09151 \[astro-ph.HE\]](#).
 - [27] A. H. Nitz, S. Kumar, Y.-F. Wang, S. Kastha, S. Wu, M. Schäfer, R. Dhurkunde, and C. D. Capano, 4-OGC: Catalog of Gravitational Waves from Compact Binary Mergers, *Astrophys. J.* **946**, 59 (2023), [arXiv:2112.06878 \[astro-ph.HE\]](#).
 - [28] A. H. Nitz, T. Dent, G. S. Davies, and I. Harry, A Search for Gravitational Waves from Binary Mergers with a Single Observatory, *Astrophys. J.* **897**, 169 (2020), [arXiv:2004.10015 \[astro-ph.HE\]](#).
 - [29] A. H. Nitz, A. Lenon, and D. A. Brown, Search for Eccentric Binary Neutron Star Mergers in the first and second observing runs of Advanced LIGO, *Astrophys. J.* **890**, 1 (2019), [arXiv:1912.05464 \[astro-ph.HE\]](#).
 - [30] A. H. Nitz and Y.-F. Wang, Search for Gravitational Waves from High-Mass-Ratio Compact-Binary Mergers of Stellar Mass and Subsolar Mass Black Holes, *Phys. Rev. Lett.* **126**, 021103 (2021), [arXiv:2007.03583 \[astro-ph.HE\]](#).
 - [31] A. H. Nitz and Y.-F. Wang, Search for gravitational waves from the coalescence of sub-solar mass and eccentric compact binaries, *Astrophys. J.* **915**, 54 (2021), [arXiv:2102.00868 \[astro-ph.HE\]](#).
 - [32] A. H. Nitz and Y.-F. Wang, Search for Gravitational Waves from the Coalescence of Subsolar-Mass Binaries in the First Half of Advanced LIGO and Virgo’s Third Observing Run, *Phys. Rev. Lett.* **127**, 151101 (2021), [arXiv:2106.08979 \[astro-ph.HE\]](#).
 - [33] A. H. Nitz and Y.-F. Wang, Broad search for gravitational waves from subsolar-mass binaries through LIGO and Virgo’s third observing run, *Phys. Rev. D* **106**, 023024 (2022), [arXiv:2202.11024 \[astro-ph.HE\]](#).
 - [34] G. S. C. Davies and I. W. Harry, Establishing significance of gravitational-wave signals from a single observatory in the PyCBC offline search, *Class. Quant. Grav.* **39**, 215012 (2022), [arXiv:2203.08545 \[gr-qc\]](#).
 - [35] R. Dhurkunde and A. H. Nitz, Search for eccentric NSBH and BNS mergers in the third observing run of Advanced LIGO and Virgo, *Phys. Rev. D* **111**, 103018 (2025), [arXiv:2311.00242 \[astro-ph.HE\]](#).
 - [36] Y.-F. Wang and A. H. Nitz, Targeted search for gravitational waves from highly spinning light compact binaries, *Mon. Not. Roy. Astron. Soc.* **528**, 3891 (2024), [arXiv:2308.16173 \[astro-ph.HE\]](#).
 - [37] K. Kacanja and A. H. Nitz, A Search for Low-mass Neutron Stars in the Third Observing Run of Advanced LIGO and Virgo, *Astrophys. J.* **984**, 61 (2025), [arXiv:2412.05369 \[astro-ph.HE\]](#).
 - [38] P. Kumar and T. Dent, Optimized search for a binary black hole merger population in LIGO-Virgo O3 data, *Phys. Rev. D* **110**, 043036 (2024), [arXiv:2403.10439 \[gr-qc\]](#).
 - [39] T. Venumadhav, B. Zackay, J. Roulet, L. Dai, and

- M. Zaldarriaga, New search pipeline for compact binary mergers: Results for binary black holes in the first observing run of Advanced LIGO, *Phys. Rev. D* **100**, 023011 (2019), [arXiv:1902.10341 \[astro-ph.IM\]](#).
- [40] T. Venumadhav, B. Zackay, J. Roulet, L. Dai, and M. Zaldarriaga, New binary black hole mergers in the second observing run of Advanced LIGO and Advanced Virgo, *Phys. Rev. D* **101**, 083030 (2020), [arXiv:1904.07214 \[astro-ph.HE\]](#).
- [41] S. Olsen, T. Venumadhav, J. Mushkin, J. Roulet, B. Zackay, and M. Zaldarriaga, New binary black hole mergers in the LIGO-Virgo O3a data, *Phys. Rev. D* **106**, 043009 (2022), [arXiv:2201.02252 \[astro-ph.HE\]](#).
- [42] A. K. Mehta, S. Olsen, D. Wadekar, J. Roulet, T. Venumadhav, J. Mushkin, B. Zackay, and M. Zaldarriaga, New binary black hole mergers in the LIGO-Virgo O3b data, *Phys. Rev. D* **111**, 024049 (2025), [arXiv:2311.06061 \[gr-qc\]](#).
- [43] D. Wadekar, J. Roulet, T. Venumadhav, A. K. Mehta, B. Zackay, J. Mushkin, S. Olsen, and M. Zaldarriaga, New black hole mergers in the LIGO-Virgo O3 data from a gravitational wave search including higher-order harmonics (2023), [arXiv:2312.06631 \[gr-qc\]](#).
- [44] B. Zackay, T. Venumadhav, L. Dai, J. Roulet, and M. Zaldarriaga, Highly spinning and aligned binary black hole merger in the Advanced LIGO first observing run, *Phys. Rev. D* **100**, 023007 (2019), [arXiv:1902.10331 \[astro-ph.HE\]](#).
- [45] B. Zackay, L. Dai, T. Venumadhav, J. Roulet, and M. Zaldarriaga, Detecting gravitational waves with disparate detector responses: Two new binary black hole mergers, *Phys. Rev. D* **104**, 063030 (2021), [arXiv:1910.09528 \[astro-ph.HE\]](#).
- [46] T. Mishra *et al.*, Search for binary black hole mergers in the third observing run of Advanced LIGO-Virgo using coherent WaveBurst enhanced with machine learning, *Phys. Rev. D* **105**, 083018 (2022), [arXiv:2201.01495 \[gr-qc\]](#).
- [47] T. Mishra, S. Bhaumik, V. Gayathri, M. J. Szczepańczyk, I. Bartos, and S. Klimenko, Gravitational waves detected by a burst search in LIGO/Virgo's third observing run, *Phys. Rev. D* **111**, 023054 (2025), [arXiv:2410.15191 \[astro-ph.HE\]](#).
- [48] R. Magee *et al.*, Sub-threshold Binary Neutron Star Search in Advanced LIGO's First Observing Run, *Astrophys. J. Lett.* **878**, L17 (2019), [arXiv:1901.09884 \[gr-qc\]](#).
- [49] Y.-J. Huang *et al.*, Scalable matched-filtering pipeline for gravitational-wave searches of compact binary mergers, *Phys. Rev. D* **112**, 082002 (2025), [arXiv:2410.16416 \[gr-qc\]](#).
- [50] S. Schmidt *et al.*, Searching for Asymmetric and Heavily Precessing Binary Black Holes in the Gravitational Wave Data from the LIGO Third Observing Run, *Phys. Rev. Lett.* **133**, 201401 (2024), [arXiv:2406.17832 \[gr-qc\]](#).
- [51] A. Menéndez-Vázquez, M. Kolstein, M. Martínez, and L. M. Mir, Searches for compact binary coalescence events using neural networks in the LIGO/Virgo second observation period, *Phys. Rev. D* **103**, 062004 (2021), [arXiv:2012.10702 \[gr-qc\]](#).
- [52] A. Menéndez-Vázquez, M. Andrés-Carcasona, M. Martínez, and L. M. Mir, Searches for compact binary coalescence events using neural networks in LIGO/Virgo third observation period, *Class. Quant. Grav.* **41**, 135018 (2024), [arXiv:2401.12912 \[gr-qc\]](#).
- [53] A. E. Koloniari, E. C. Koursoumpa, P. Nousi, P. Lampropoulos, N. Passalis, A. Tefas, and N. Stergioulas, New gravitational wave discoveries enabled by machine learning, *Mach. Learn. Sci. Tech.* **6**, 015054 (2025), [arXiv:2407.07820 \[gr-qc\]](#).
- [54] E. Marx *et al.*, Machine-learning pipeline for real-time detection of gravitational waves from compact binary coalescences, *Phys. Rev. D* **111**, 042010 (2025), [arXiv:2403.18661 \[gr-qc\]](#).
- [55] E. Marx *et al.*, Machine learning-enabled search for binary black hole mergers in LIGO-Virgo-KAGRA's third observing run, *Phys. Rev. D* **112**, 043007 (2025), [arXiv:2505.21261 \[astro-ph.IM\]](#).
- [56] E. A. Moreno *et al.*, Neural network-based search for unmodeled transients in LIGO-Virgo-KAGRA's third observing run, *Phys. Rev. D* **112**, 022003 (2025), [arXiv:2412.19883 \[gr-qc\]](#).
- [57] D. Beveridge, A. McLeod, L. Wen, and A. Wicenec, Novel deep learning approach to detecting binary black hole mergers, *Phys. Rev. D* **111**, 024005 (2025), [arXiv:2308.08429 \[gr-qc\]](#).
- [58] A. McLeod, D. Beveridge, L. Wen, and A. Wicenec, Binary neutron star merger search pipeline powered by deep learning, *Phys. Rev. D* **111**, 024035 (2025), [arXiv:2409.06266 \[gr-qc\]](#).
- [59] R. Abbott *et al.* (KAGRA, VIRGO, LIGO Scientific), Open Data from the Third Observing Run of LIGO, Virgo, KAGRA, and GEO, *Astrophys. J. Suppl.* **267**, 29 (2023), [arXiv:2302.03676 \[gr-qc\]](#).
- [60] B. Allen *et al.*, FINDCHIRP: An Algorithm for detection of gravitational waves from inspiraling compact binaries, *Phys. Rev. D* **85**, 122006 (2012), [arXiv:gr-qc/0509116](#).
- [61] D. Mukherjee *et al.*, Template bank for spinning compact binary mergers in the second observation run of Advanced LIGO and the first observation run of Advanced Virgo, *Phys. Rev. D* **103**, 084047 (2021).
- [62] Q. Chu *et al.*, SPIIR online coherent pipeline to search for gravitational waves from compact binary coalescences, *Phys. Rev. D* **105**, 024023 (2022), [arXiv:2011.06787 \[gr-qc\]](#).
- [63] L. S. Collaboration, V. Collaboration, and K. Collaboration, Gwtc-3: Compact binary coalescences observed by ligo and virgo during the second part of the third observing run — o3 search sensitivity estimates, [10.5281/zenodo.7890437](#) (2023).
- [64] A. Bohé *et al.*, Improved effective-one-body model of spinning, nonprecessing binary black holes for the era of gravitational-wave astrophysics with advanced detectors, *Phys. Rev. D* **95**, 044028 (2017), [arXiv:1611.03703 \[gr-qc\]](#).
- [65] N. Christensen, P. Shawhan, G. González, and (for the LIGO Scientific Collaboration), Vetoes for inspiral triggers in LIGO data, *Classical and Quantum Gravity* **21**, S1747 (2004).
- [66] LIGO Scientific Collaboration, [GraceDB — The Gravitational-Wave Candidate Event Database](#).
- [67] F. Robinet, N. Arnaud, N. Leroy, A. Lundgren, D. Macleod, and J. McIver, Omicron: a tool to characterize transient noise in gravitational-wave detectors, *SoftwareX* **12**, 100620 (2020), [arXiv:2007.11374 \[astro-ph.IM\]](#).
- [68] S. Ossokine *et al.*, Multipolar effective-one-body wave-

- forms for precessing binary black holes: Construction and validation, *Phys. Rev. D* **102**, 044055 (2020).
- [69] M. Abadi *et al.*, *TensorFlow: Large-scale machine learning on heterogeneous systems* (2015), software available from tensorflow.org.
- [70] Y. LeCun *et al.*, Backpropagation Applied to Handwritten Zip Code Recognition, *Neural Computation* **1**, 541 (1989).
- [71] K. He *et al.*, Deep Residual Learning for Image Recognition [10.1109/CVPR.2016.90](https://arxiv.org/abs/1512.03385) (2015), [arXiv:1512.03385 \[cs.CV\]](https://arxiv.org/abs/1512.03385).
- [72] ONNX Runtime developers, ONNX Runtime, <https://onnxruntime.ai/> (2021), version: 1.17.0.
- [73] S. S. Chaudhary *et al.*, Low-latency gravitational wave alert products and their performance at the time of the fourth LIGO-Virgo-KAGRA observing run, *Proc. Nat. Acad. Sci.* **121**, e2316474121 (2024), [arXiv:2308.04545 \[astro-ph.HE\]](https://arxiv.org/abs/2308.04545).
- [74] W. M. Farr, J. R. Gair, I. Mandel, and C. Cutler, Counting And Confusion: Bayesian Rate Estimation With Multiple Populations, *Phys. Rev. D* **91**, 023005 (2015), [arXiv:1302.5341 \[astro-ph.IM\]](https://arxiv.org/abs/1302.5341).
- [75] S. J. Kapadia *et al.*, A self-consistent method to estimate the rate of compact binary coalescences with a Poisson mixture model, *Class. Quant. Grav.* **37**, 045007 (2020), [arXiv:1903.06881 \[astro-ph.HE\]](https://arxiv.org/abs/1903.06881).
- [76] B. F. Schutz, Networks of gravitational wave detectors and three figures of merit, *Class. Quant. Grav.* **28**, 125023 (2011), [arXiv:1102.5421 \[astro-ph.IM\]](https://arxiv.org/abs/1102.5421).
- [77] H.-Y. Chen and D. E. Holz, The Loudest Gravitational Wave Events (2014), [arXiv:1409.0522 \[gr-qc\]](https://arxiv.org/abs/1409.0522).
- [78] B. P. Abbott *et al.* (LIGO Scientific, Virgo), Supplement: The Rate of Binary Black Hole Mergers Inferred from Advanced LIGO Observations Surrounding GW150914, *Astrophys. J. Suppl.* **227**, 14 (2016), [arXiv:1606.03939 \[astro-ph.HE\]](https://arxiv.org/abs/1606.03939).
- [79] A. Buikema *et al.* (aLIGO), Sensitivity and performance of the Advanced LIGO detectors in the third observing run, *Phys. Rev. D* **102**, 062003 (2020), [arXiv:2008.01301 \[astro-ph.IM\]](https://arxiv.org/abs/2008.01301).
- [80] N. Nagarajan and C. Messenger, Identifying and mitigating machine-learning biases for the gravitational-wave detection problem, *Phys. Rev. D* **112**, 103002 (2025), [arXiv:2501.13846 \[gr-qc\]](https://arxiv.org/abs/2501.13846).
- [81] D. Williams, Beyond GWTC-3: analyzing and verifying new gravitational-wave events from community catalogues, *Class. Quant. Grav.* **42**, 105012 (2025), [arXiv:2401.08709 \[astro-ph.HE\]](https://arxiv.org/abs/2401.08709).
- [82] R. Essick *et al.*, iDQ: Statistical inference of non-gaussian noise with auxiliary degrees of freedom in gravitational-wave detectors, *Machine Learning: Science and Technology* **2**, 015004 (2020).
- [83] L. S. Collaboration and V. Collaboration, Gwtc-2.1: Deep extended catalog of compact binary coalescences observed by ligo and virgo during the first half of the third observing run - data quality products for gw searches, [10.5281/zenodo.6477646](https://arxiv.org/abs/2205.09717) (2022).
- [84] A. H. Nitz, T. Dal Canton, D. Davis, and S. Reyes, Rapid detection of gravitational waves from compact binary mergers with PyCBC Live, *Phys. Rev. D* **98**, 024050 (2018), [arXiv:1805.11174 \[gr-qc\]](https://arxiv.org/abs/1805.11174).
- [85] L. S. Collaboration and V. Collaboration, Gwtc-2.1: Deep extended catalog of compact binary coalescences observed by ligo and virgo during the first half of the third observing run - candidate data release, [10.5281/zenodo.5759108](https://arxiv.org/abs/2205.09717) (2021).
- [86] L. S. Collaboration, V. Collaboration, and K. Collaboration, Gwtc-3: Compact binary coalescences observed by ligo and virgo during the second part of the third observing run — candidate data release, [10.5281/zenodo.5546665](https://arxiv.org/abs/2205.09717) (2021).
- [87] D. Williams, J. Veitch, M. Chiofalo, P. Schmidt, R. Udall, A. Vajpeyi, and C. Hoy, Asimov: A framework for coordinating parameter estimation workflows, *The Journal of Open Source Software* **8**, 4170 (2023), [arXiv:2207.01468 \[gr-qc\]](https://arxiv.org/abs/2207.01468).
- [88] D. Williams, D. Macleod, A. Vajpeyi, J. Clark, and R. O’Shaughnessy, *transientlunatic/asimov: v0.5.8* (2024).
- [89] N. J. Cornish and T. B. Littenberg, Bayeswave: Bayesian inference for gravitational wave bursts and instrument glitches, *Classical and Quantum Gravity* **32**, 135012 (2015), [arXiv:1410.3835 \[gr-qc\]](https://arxiv.org/abs/1410.3835).
- [90] T. B. Littenberg and N. J. Cornish, Bayesian inference for spectral estimation of gravitational wave detector noise, *Phys. Rev. D* **91**, 084034 (2015).
- [91] G. Ashton *et al.*, BILBY: A user-friendly Bayesian inference library for gravitational-wave astronomy, *Astrophys. J. Suppl.* **241**, 27 (2019), [arXiv:1811.02042 \[astro-ph.IM\]](https://arxiv.org/abs/1811.02042).
- [92] J. S. Speagle, dynesty: a dynamic nested sampling package for estimating Bayesian posteriors and evidences, *Mon. Not. Roy. Astron. Soc.* **493**, 3132 (2020), [arXiv:1904.02180 \[astro-ph.IM\]](https://arxiv.org/abs/1904.02180).
- [93] G. Pratten *et al.*, Computationally efficient models for the dominant and subdominant harmonic modes of precessing binary black holes, *Phys. Rev. D* **103**, 104056 (2021), [arXiv:2004.06503 \[gr-qc\]](https://arxiv.org/abs/2004.06503).
- [94] C. Hoy and V. Raymond, PESummary: the code agnostic Parameter Estimation Summary page builder, *SoftwareX* **15**, 100765 (2021), [arXiv:2006.06639 \[astro-ph.IM\]](https://arxiv.org/abs/2006.06639).
- [95] A. K. Mehta, A. Buonanno, J. Gair, M. C. Miller, E. Farag, R. J. deBoer, M. Wiescher, and F. X. Timmes, Observing Intermediate-mass Black Holes and the Upper Stellar-mass gap with LIGO and Virgo, *Astrophys. J.* **924**, 39 (2022), [arXiv:2105.06366 \[gr-qc\]](https://arxiv.org/abs/2105.06366).
- [96] W. A. Fowler and F. Hoyle, Neutrino Processes and Pair Formation in Massive Stars and Supernovae, *Astrophys. J. Suppl.* **9**, 201 (1964).
- [97] Z. Barkat, G. Rakavy, and N. Sack, Dynamics of Supernova Explosion Resulting from Pair Formation, *Phys. Rev. Lett.* **18**, 379 (1967).
- [98] C. L. Fryer, S. E. Woosley, and A. Heger, Pair instability supernovae, gravity waves, and gamma-ray transients, *Astrophys. J.* **550**, 372 (2001), [arXiv:astro-ph/0007176](https://arxiv.org/abs/astro-ph/0007176).
- [99] K. Belczynski *et al.*, The Effect of Pair-Instability Mass Loss on Black Hole Mergers, *Astron. Astrophys.* **594**, A97 (2016), [arXiv:1607.03116 \[astro-ph.HE\]](https://arxiv.org/abs/1607.03116).
- [100] M. Spera and M. Mapelli, Very massive stars, pair-instability supernovae and intermediate-mass black holes with the SEVN code, *Mon. Not. Roy. Astron. Soc.* **470**, 4739 (2017), [arXiv:1706.06109 \[astro-ph.SR\]](https://arxiv.org/abs/1706.06109).
- [101] S. Stevenson, M. Sampson, J. Powell, A. Vigna-Gómez, C. J. Neijssel, D. Szécsi, and I. Mandel, The impact of pair-instability mass loss on the binary black hole mass distribution, *The Astrophysical Journal* **882**, 121 (2019).

- [102] G. Costa, A. Bressan, M. Mapelli, P. Marigo, G. Iorio, and M. Spera, Formation of GW190521 from stellar evolution: the impact of the hydrogen-rich envelope, dredge-up and $^{12}\text{C}(\alpha, \gamma)^{16}\text{O}$ rate on the pair-instability black hole mass gap, *Mon. Not. Roy. Astron. Soc.* **501**, 4514 (2021), [arXiv:2010.02242 \[astro-ph.SR\]](#).
- [103] R. Farmer, M. Renzo, S. de Mink, M. Fishbach, and S. Justham, Constraints from gravitational wave detections of binary black hole mergers on the $^{12}\text{C}(\alpha, \gamma)^{16}\text{O}$ rate, *Astrophys. J. Lett.* **902**, L36 (2020), [arXiv:2006.06678 \[astro-ph.HE\]](#).
- [104] M. Renzo, R. Farmer, S. Justham, Y. Götberg, S. E. de Mink, E. Zapartas, P. Marchant, and N. Smith, Predictions for the hydrogen-free ejecta of pulsational pair-instability supernovae, *Astron. Astrophys.* **640**, A56 (2020), [arXiv:2002.05077 \[astro-ph.SR\]](#).
- [105] R. Abbott *et al.* (LIGO Scientific, VIRGO, KAGRA), Search for intermediate-mass black hole binaries in the third observing run of Advanced LIGO and Advanced Virgo, *Astron. Astrophys.* **659**, A84 (2022), [arXiv:2105.15120 \[astro-ph.HE\]](#).